TU Delft

Delft University of Technology

Document Version
Final published version

Licence
CC BY

Citation (APA)
Shakeri, I., Seidel, M., Tankova, T., & Veljkovic, M. (2026). Fatigue assessment of bolted L-flange connections considering preload loss and local bending: Experimental investigation and fracture-mechanics-based analysis. *International Journal of Fatigue*, *213*, Article 109887. https://doi.org/10.1016/j.ijfatigue.2026.109887

Important note
To cite this publication, please use the final published version (if applicable).
Please check the document version above.

Copyright
In case the licence states “Dutch Copyright Act (Article 25fa)”, this publication was made available Green Open Access via the TU Delft Institutional Repository pursuant to Dutch Copyright Act (Article 25fa, the Taverne amendment). This provision does not affect copyright ownership.
Unless copyright is transferred by contract or statute, it remains with the copyright holder.

Sharing and reuse
Other than for strictly personal use, it is not permitted to download, forward or distribute the text or part of it, without the consent of the author(s) and/or copyright holder(s), unless the work is under an open content license such as Creative Commons.

Takedown policy
Please contact us and provide details if you believe this document breaches copyrights.
We will remove access to the work immediately and investigate your claim.

This work is downloaded from Delft University of Technology.

International Journal of Fatigue 213 (2026) 109887

Contents lists available at ScienceDirect

International Journal of Fatigue

journal homepage: www.elsevier.com/locate/ijfatigue

Fatigue assessment of bolted L-flange connections considering preload loss and local bending: Experimental investigation and fracture-mechanics-based analysis

Iman Shakeri [a,*], Marc Seidel [b], Trayana Tankova [a], Milan Veljkovic [a]

[a] Department of Engineering Structures, Delft University of Technology, 2628CN Delft, the Netherlands
[b] Siemens Gamesa Renewable Energy Deutschland GmbH, Hamburg, Germany

ARTICLE INFO

Keywords:
Fatigue life
Bolt, S-N curve
Fatigue crack growth
L-flange connection
Preload
Stress intensity factor

ABSTRACT

In wind turbine towers, bolted flange connections are subjected to repeated cyclic loading, making fatigue a critical concern for structural integrity. This study experimentally and numerically investigates the fatigue behaviour of M48 bolted L-flange connections subjected to high preload introduced by tension-tightening. The preload initially reached approximately 95% of the bolt yield strength and stabilised at approximately 79% after tensioner removal. A total of 12 full-scale fatigue tests were conducted to quantify the influence of combined axial and bending loading, as well as preload relaxation during cyclic loading. The results show that high preload significantly improves fatigue life, particularly in the endurance-limit region, where existing design standards provide overly conservative predictions. Cyclic loading was found to accelerate preload relaxation, resulting in an increase in the tensile stress range in the bolt. To account for both bending effects and preload loss, an equivalent effective stress range was proposed, which reduced scatter in the fatigue data and provided a more consistent fatigue-damage parameter. In addition, a three-dimensional fracture-mechanics-based fatigue crack growth framework was developed to predict fatigue life. Bolt preload was introduced in the finite element model using a thermo-mechanical approach, and the model was validated against experimental results. Fatigue crack growth parameters were obtained from dedicated tests on specimens extracted from the bolt material. The numerically predicted S-N curves showed good agreement with experimental results and standard-based predictions in the finite-life regime. The proposed methodology improves fatigue-life prediction and supports more reliable design guidelines for preloaded wind turbine flange connections.

1. Introduction

Wind turbine towers are increasingly being constructed with ever-larger hub heights and rotor diameters, driven by the rising global demand for renewable energy and the economic advantages of scaling offshore wind systems [1]. As turbine capacity increases, so does the demand placed on structural connections, particularly the bolted L-flange connections that join tower segments and transfer complex loads (Fig. 1a). These connections, which rely on threaded high-strength bolts to maintain structural integrity, are repeatedly subjected to millions of load cycles over their service life. Fatigue damage, therefore, becomes a dominant and governing design consideration. Local stress concentrations at the thread root, combined with fluctuating axial and bending stresses, make these connections particularly challenging to predict for crack initiation and growth. Ensuring adequate fatigue performance is thus essential not only for preventing catastrophic failures but also for reducing maintenance costs and improving the long-term reliability of wind turbine support structures.

One of the central factors influencing the fatigue behaviour of bolted connections is the bolt preload. It establishes the clamping force that governs load transfer between the connected flanges, as illustrated in Fig. 1b. When an adequate preload is applied, most external loads are transmitted through variations in compressive stress between the connecting surfaces, thereby protecting the bolt from large stress fluctuations. Conversely, insufficient or uneven preload between bolts in the ring flange connection increases the bolt load amplitude and accelerates fatigue damage. The load transfer function (LTF) characterises how the

* Corresponding author.
E-mail addresses: I.Shakeri-1@tudelft.nl, iman.shakeri1368@gmail.com (I. Shakeri), marc.seidel@siemensgamesa.com (M. Seidel), T.Tankova@tudelft.nl (T. Tankova), M.Veljkovic@tudelft.nl (M. Veljkovic).

https://doi.org/10.1016/j.ijfatigue.2026.109887
Received 14 May 2026; Received in revised form 3 July 2026; Accepted 23 July 2026
Available online 26 July 2026
0142-1123/© 2026 The Author(s). Published by Elsevier Ltd. This is an open access article under the CC BY license (http://creativecommons.org/licenses/by/4.0/).

Nomenclature

A	Constant of S-N curve
A_{min}	Cross-sectional area of stud minor diameter
A_s	Tensile-stress area
A_{ut}	Cross-sectional area of stud unthreaded section
a	Crack depth
a_c	Critical crack length
a_f	Distance from the flange inner face to the bolt-hole
a_i	Initial crack depth
B	Thickness of ESET specimen
b	Fatigue strength exponent
b_f	Distance from the bolt-hole to the shell mid-surface
C	Material parameter in Paris equation
c	Crack surface half-length
c'	Fatigue ductility exponent
c_i	Initial crack surface half-length
D_A	Equivalent diameter at the clamped parts interface
$D_{A,Gr}$	Limiting diameter of the deformation cone
D_{maj}	Stud major diameter
D_{min}	Stud minor diameter
D_{nom}	Stud nominal diameter
D_{ref}	Stud reference diameter
D_{ut}	Diameter of stud unthreaded section
DC_{mean}	Mean detail category
DC_{Table}	Design (characteristic) detail category
d_h	Diameter of bolt-hole
d_W	Bearing diameter under the nut
E	Young's modulus
E_p	Young's modulus of the clamped parts
E_s	Young's modulus of the stud
F	Force
F_b	Bolt/stud force
F_{ext}	External force applied to the flange segment
F_{max}	Maximum force
F_{min}	Minimum force
F_{PL}	Bolt/stud force caused by preload
F_Y	Axial force along the Y-axis
f_u	Ultimate strength
f_y	Yield stress
J_{int}	Interaction integral
K_{I}	Stress intensity factor of mode I
K_{II}	Stress intensity factor of mode II
K_{III}	Stress intensity factor of mode III
k_b	Bending reduction factor
k_m	Adjustment factor from design to mean curve
k_s	Size factor
L	Stud length
l_H	Length of the deformation sleeve
l_K	Total clamping length
l_{th}	Threaded length of stud within the clamping length
l_{ut}	Unthreaded length of stud
l_V	Length of the deformation cone
M_b	Bending moment in bolt/stud
M_Z	Bending moment around Z-axis
m	Inverse slope of S-N curve
N	Number of cycles
N_f	Number of cycles to failure
N_{ini}	Fatigue crack initiation life
N_{pro}	Fatigue crack propagation life
n	Material parameter in Paris equation
n'	Cyclic strain-hardening exponent
P	Thread pitch
P_J	Vormwald damage parameter
R	Load ratio
R_b	Stud radius of unthreaded section
R_{ext}	External load ratio applied to the flange segment
R_{th}	Thread root radius
S_f	Strain amplification factor
s	Thickness of L-flange shell
t	Thickness of L-flange
t_l	Tolerance limit factor
W	Width of ESET specimen
w	Width of L-flange
w_s	Width of segment
Y_{A}	Dimensionless factor for axial force
Y_{B}	Dimensionless geometry factor for bending
y	Dimensionless geometric parameter
α_s	Size-effect exponent
β_L	Dimensionless geometric parameter
ΔF	Force range
ΔF_{b}	Bolt force range
ΔF_{ext}	External force range
ΔK_{I}	Mode I stress intensity factor range
$\Delta\varepsilon_{loc}$	Total strain range at the thread root
$\Delta\varepsilon_{p,loc,eff}$	Local plastic strain range at the thread root
$\Delta\sigma$	Nominal stress range
$\Delta\sigma_A$	Stress range from axial force in the stud
$\Delta\sigma_B$	Stress range from bending moment in the stud
$\Delta\sigma_{eff}$	Bolt/stud effective stress range
$\Delta\sigma_{eq}$	Equivalent stress range
$\Delta\sigma_{loc,eff}$	Local effective stress range at thread root
$\Delta\sigma_{max}$	Maximum stress range
δ_p	Resilience of the clamped parts
δ_s	Resilience of the stud
ε	Measured strain from strain gauge
ε_f'	Fatigue ductility coefficient
θ	Angle of strain gauge in regards to x' axis
λ	Plane strain/stress factor
ν	Poisson's ratio
σ_A	Bolt/stud axial stress
σ_B	Bolt/stud bending stress
σ_f'	Fatigue strength coefficient
$\sigma_{\mathrm{loc,max}}$	Local maximum stress at the thread root
$\sigma_{\mathrm{loc,min}}$	Local minimum stress at the thread root
$\widehat{\sigma}_{\log N}$	Standard deviation of log$N$
σ_{PL}	Bolt/stud preload stress
φ_D	Deformation-cone angle

external load applied to a segment of the tower shell, F_{ext}, is transmitted to the bolt as F_b, as illustrated schematically in Fig. 1c. In an ideal flange configuration, bolt tightening introduces the contact pressure between the flange surfaces, producing an axial clamping force aligned with the bolt axis (Fig. 1b). This clamping force counteracts the applied preload. When an external load is applied, the path through which it is transferred to the bolt is nonlinear [2,3]. An external load relieves the existing clamp force and is partially transferred by the bolt. The LTF shape depends on the stiffness ratio between the flanges and bolts, and the pretension stress level.

Several researchers have explored how bolt preload influences the behaviour of flange connections [4–6]. Schaumann and Seidel [7]

investigated failure mechanisms in steel flange connections and showed that accurate application of preload is essential for reliable load transmission and improved fatigue resistance. Further work by Seidel [5] examined fatigue loading in ring-flange systems, underscoring the importance of preload in controlling stress distribution during operation. Mehmanparast et al. [8] provided an overview of fatigue-related issues in offshore wind turbine bolted connections and identified preload optimisation as a crucial measure to prevent early-stage failures. Although the application of high preload levels may induce noticeable plastic deformation, previous studies have reported that such deformation does not adversely affect the structural performance of the connection when it remains temporary, as the associated reduction in ultimate load capacities is generally negligible [9,10]. Jian et al. [11] experimentally demonstrated bolt failure after the clamped forces were exceeded. Shahani and Shakeri [12] carried out axial fatigue tests to study the influence of preload on the endurance limit of bolts. Their findings revealed that the elevated mean stress arising from larger preload levels does not diminish the endurance limit, mainly due to local plasticity occurring at the thread root. Glienke et al. [13] and Maljaars & Euler [14] assessed the roles of size and mean stress on bolt fatigue performance and noted that existing standards exhibit considerable differences in their fatigue provisions. This inconsistency is partly attributed to insufficient design guidance for bolts fabricated from various materials and assembled under diverse conditions [15], as well as the limited availability of experimental data for bolts subjected to high mean stress levels [14].

Despite its importance, achieving a precise and uniform preload in large-diameter bolts is challenging due to tightening uncertainties, geometric imperfections, and manufacturing tolerances [16,17]. Moreover, preload is not constant throughout operation: significant preload relaxation commonly occurs during the early cycles of turbine operation due to embedment, micro-slip, thread seating, and localised plasticity in the bolt or flange [18,19]. This preload loss increases the effective stress range in the bolt, directly impacting fatigue life [20]. Zou et al. [17] reviewed factors influencing the fatigue evaluation of flange connections in floating wind turbine towers. Their review indicated that large-diameter bolts in these connections are prone to losing a portion of their initial pretension due to vibration effects occurring during installation or service. Such preload loss due to settlements, can elevate the cyclic stress range of the bolts, ultimately accelerating fatigue damage and shortening the overall fatigue life [5]. Although standards [18,21,22] increasingly acknowledge the importance of preload, there is still a lack of explicit guidance regarding its evolution under service conditions and the implications for fatigue prediction in L-flange connections.

Another critical factor in fatigue assessment of bolts that is often overlooked is the bending effect that results from unavoidable load eccentricities in the tower-shell geometry, manufacturing deviations in flange flatness, bolt alignment, and shell roundness. Even small eccentricities can create substantial bending moments in the bolts, significantly increasing the local stress range [23]. Current fatigue design standards such as DNV-RP-C203 (DNV) [21] and Eurocode 3 Part 1-9 (EC3) [22] do not explicitly incorporate the combined influence of preload variation and bending-induced stresses for L-flange connections. Lochan et al. [24] conducted a review of fatigue behaviour in bolted connections used in offshore wind turbines, emphasizing the shortcomings of existing design standards and the necessity for more advanced and realistic fatigue assessment approaches. Schwarz et al. [25] showed through experimental investigations that ignoring bending-induced stresses in L-flange assemblies results in a substantial overestimation of fatigue life when predictions are based on fatigue data derived from purely axial bolt-nut loading conditions. In EC3 [22], the detail category assigned to bolts is reduced when bending effects are not explicitly considered. While newer guidelines such as IEC 61400-6 (IEC) [18] have advanced the understanding of bolt force and moment

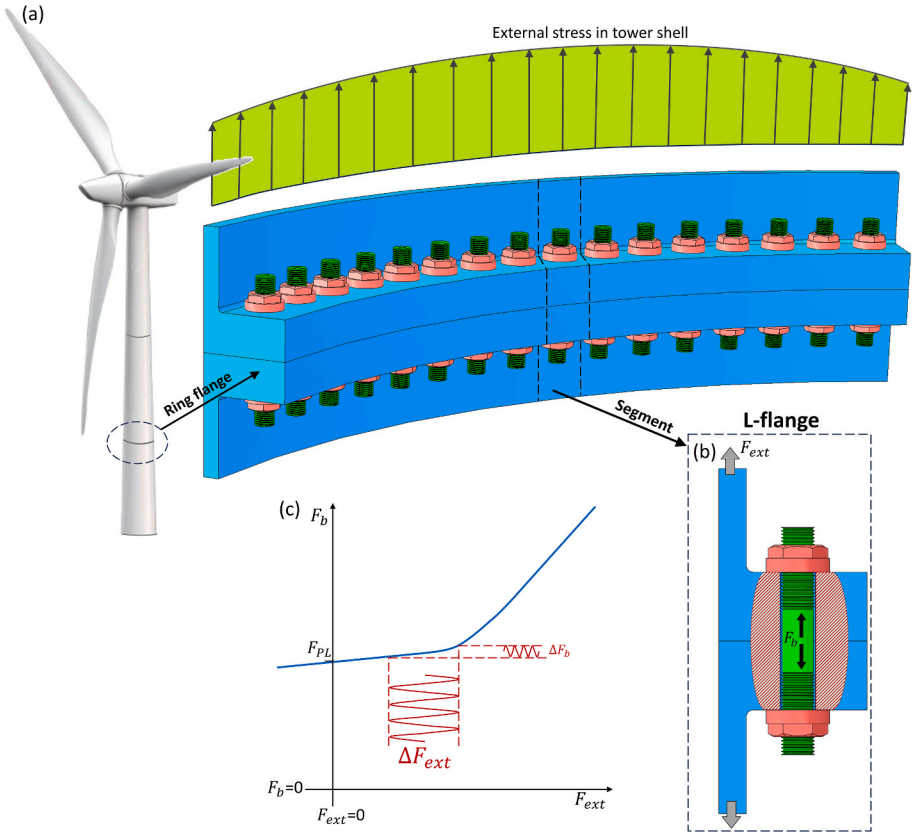

Fig. 1. (a) Schematic view of a ring flange connection used in a tower of wind turbine (modified from [2]) (b) geometry of an L-flange connection, (c) Load transfer process assuming ideal alignment between flange surfaces (based on [3]).

distribution, they still provide limited formulation for incorporating bending in high-preload conditions into fatigue-life assessment. The missing knowledge should be addressed through refined methodologies that capture the interactions between actual preload level, bolt bending, and cyclic loading.

Finite element analysis (FEA) has become an indispensable tool for addressing the complex behaviour of large bolted connections [26,27], offering the capability to model contact interactions [28,29], thread geometry [30,31], load transfer mechanisms [32,33] and stress redistributions [34,35]. Detailed 3D FEA enables the examination of nonlinear effects such as bolt-flange contact behaviour, stress concentration evolution, stresses introduced during tightening, and local plasticity. Numerous studies have utilised numerical simulations to assess ring-flange performance [4–6], preload loss mechanisms [36,37], and geometric imperfections [3,38]. However, many existing models simplify the bolt geometry, neglect contact nonlinearities, or omit the interaction between preload reduction and bending. Wegener et al. [36,37] performed numerical studies on full ring flange assemblies, focusing on preload reduction caused by single overloads and plastic deformation occurring in either the flange or the bolt. Cheng et al. [39] carried out detailed FEA of ring flange connections, identifying key stress concentrations and deformation modes across different loading scenarios. These investigations highlight the capability of FEA to capture the complex interplay between preload conditions and cyclic loading, thereby supporting more reliable design improvements and maintenance planning.

The Global S-N-based approach [40–42], commonly adopted in design standards, does not explicitly account for crack growth behaviour or stress redistribution as fatigue damage accumulates. In contrast, fracture-mechanics-based approaches provide a physically based framework for modelling fatigue damage and have been widely applied to structural and offshore components. For example, He et al. [43,44] demonstrated their effectiveness in predicting fatigue crack growth (FCG) in offshore structures, including mooring systems and submerged fishing farm platforms. These studies highlighted the capability of fracture mechanics to quantify the influence of crack size, shape and location on structural integrity and fatigue life, particularly under complex loading conditions where conventional S-N methods is based on oversimplified assumptions. In the context of threaded connections, FCG modelling combined with detailed stress intensity factor (SIF) evaluation has shown significant potential for improving fatigue-life predictions. Prior research [20] have demonstrated that the SIFs of large-diameter bolts are highly sensitive to crack depth, initial crack location, thread geometry, bending effects, and preload level. Therefore, fracture-mechanics-based approaches combined with detailed FEA offer a promising route for achieving accurate and physically consistent fatigue-life predictions of preloaded L-flange connections.

Several studies [45–47] have employed fracture mechanics approaches to investigate high-strength bolts, with most focusing on simple axial loading conditions. Very limited attention has been focused on how preloaded bolts under axial-bending interaction influence 3D crack propagation in large-diameter bolts in L-flange applications. Moreover, comprehensive experimental programmes investigating crack growth parameters for high-strength bolts at high mean stress are scarce, leading to significant uncertainty in numerical predictions. Addressing these gaps requires combining experimental investigations, detailed 3D FEA, and FCG simulations to develop a robust framework that accurately predicts the fatigue life of eccentrically loaded, preloaded flange connections.

The current study investigates the effect of combined axial and bending loading on the fatigue life of bolts in preloaded L-flange connections. Full-scale fatigue tests are carried out on M48 bolted L-flange segments to capture the influence of bending stresses arising from load eccentricity on fatigue behaviour. In addition, bolt preload loss is measured both prior to and during cyclic loading. A detailed three-dimensional FCG analysis based on fracture mechanics is then performed on the preloaded L-flange connection to predict fatigue life. A new and efficient approach for inducing bolt preload using thermo-mechanical analysis is developed, and the finite element (FE) model is validated against experimental measurements. The experimental and numerical results are further compared with existing design standards, and an improved framework for predicting S-N curves that accounts for bending effects and preload variation is proposed. The novel findings of this study advance fatigue life prediction methodologies for L-flange connections, support the development of improved design guidelines, and enhance the long-term reliability of preloaded bolted connections in wind turbine towers, with applicability to a wider range of similar structural systems.

2. Methodology

The experimental and numerical approaches are used to investigate the fatigue behaviour of an eccentrically loaded, highly preloaded M48 bolted L-flange connection. The experimental programme includes material-property testing, full-scale fatigue segment test setup, monitoring of preloading procedure, and instrumentation used to measure axial force and bending moments in the stud. In addition, tailor-made FCG tests performed on specimens extracted from the bolt material are also introduced to obtain the crack growth parameters required for numerical analysis. Subsequently, the FE modelling strategy is developed to incorporate material modelling, contact definitions, model the preload of bolt by a thermo-mechanical approach, and external loading. The three-dimensional fracture-mechanics-based FCG framework is developed, including the global-local submodelling strategy, crack initiation assumptions, adaptive remeshing technique, SIF evaluation and numerical integration procedure used to predict fatigue life.

2.1. L-flange fatigue experiment

2.1.1. Material data and fatigue test setup

The ring flange is simplified by considering a single-stud segment model in which the global axial shell load is equally shared among all studs, an approach widely accepted [2,17–20,23,25,30,48] for capturing the governing stress state in the critical stud. Fig. 2a shows the segment of the L-flange connection used in this investigation. The flanges were machined from a 140 mm thick S355J2+N steel plate to the dimensions shown in Fig. 2b, representing typical tower flange dimensions for wind turbines. The material properties provided by the fabricator show a yield strength of 343 MPa and an ultimate tensile strength of 511 MPa.

The bolted assembly consisted of an M48 partially threaded stud (i.e. a headless threaded fastener), hot-dip galvanised (HDG) and thread-rolled after heat treatment (Fig. 2c), in combination with ISR nuts (Fig. 2d). Both the stud and nut were of strength class 10.9 with a nominal thread pitch of $P = 5$ mm. The unthreaded section has a diameter of $D_{ut} = 45$ mm, and the tensile stress area used for stress calculations in the threaded part is A_s=1470 mm^2.

The chemical compositions of the materials used in the connection components are given in Table 1. To determine the stud material properties, tensile tests were performed in accordance with ISO 6892 [49] on three circular coupon specimens with a diameter of 10 mm. The specimens were extracted from the threaded portion of the stud, as close as practicable to the outer surface as shown in Fig. 2c, to obtain material properties representative of the material surrounding the thread root where the crack initiated based on experimental evidence. The measured mechanical properties of the stud are listed in Table 2. According to ISO 898-1 [50], property class 10.9 fasteners are required to have a minimum yield strength of 940 MPa and a minimum ultimate tensile strength of 1040 MPa. The experimentally measured values exceed these requirements, confirming compliance with the specified property class and demonstrating that the material properties are representative of high-strength class 10.9 studs used in wind turbine tower flange connections.

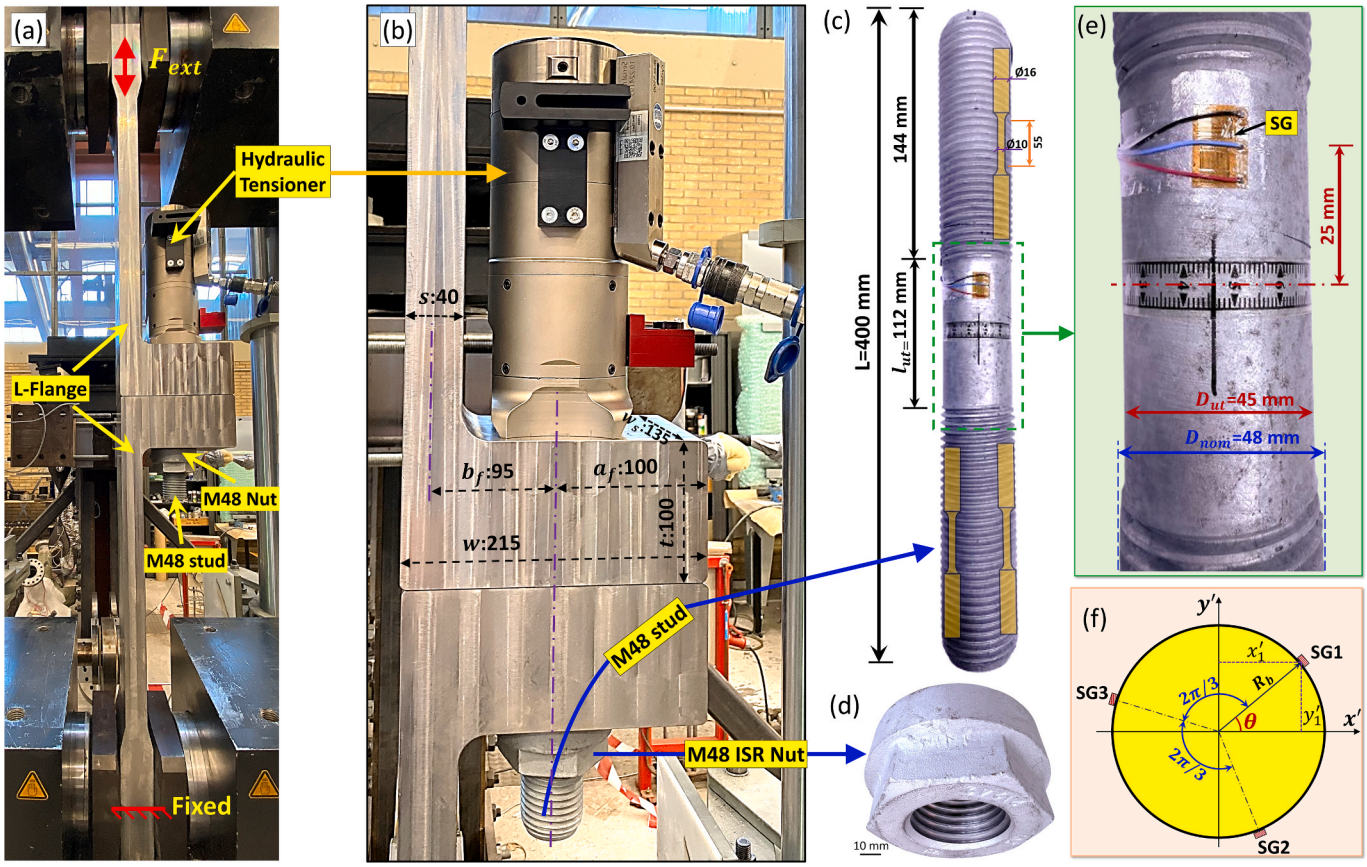

Fig. 2. (a) Fatigue test setup for the L-flange connection segment; (b) application of a hydraulic tensioner for stud preloading (dimensions in mm); (c) M48 partially threaded HDG stud and schematically shown the locations of tensile specimens; (d) M48 ISR nut; (e) SG glued to the unthreaded portion of the stud; (f) circumferential arrangement of SGs at 120° intervals in the local $x'-y'$ coordinate system.

Table 1
Chemical composition (wt%) of parts used for the connection.

Part	C	Si	Mn	S	P	Cr	Ni	Mo	Al	Cu	Nb
Flange	0.16	0.188	1.445	0.003	0.009	0.025	0.021	0.001	0.054	0.038	0.029
Stud	0.31	0.18	0.85	0.009	0.006	1.14	0.07	0.01	0.032	-	-
Nut	0.39	0.24	0.64	0.01	0.022	0.892	-	-	-	-	-

Table 2
Mechanical properties of the stud material 10.9.

f_y 0.2% (MPa)	f_u(MPa)	E(GPa)	Elongation (%)
1014.6 ± 3.6	1105.1 ± 27.3	210.1 ± 3.1	15.6 ± 0.7

bending stresses, three SGs were positioned circumferentially at 120° intervals around the stud surface, as illustrated in Fig. 2f. This configuration allows the calculation of the axial force and bending moment components using Eq. (1), which is derived in detail in Appendix A.

$$\begin{bmatrix} F_b \\ M_{x'} \\ M_{y'} \end{bmatrix} = EA_{ut} \begin{bmatrix} \frac{1}{3} & \frac{1}{3} & \frac{1}{3} \\ \frac{D_{ut}\sqrt{3}}{36}\left(-\cos\left(\theta+\frac{\pi}{3}\right)+\sin\left(\theta+\frac{\pi}{6}\right)\right) & \frac{D_{ut}\sqrt{3}}{36}\left(-\cos(\theta)-\sin\left(\theta+\frac{\pi}{6}\right)\right) & \frac{D_{ut}\sqrt{3}}{36}\left(\cos\left(\theta+\frac{\pi}{3}\right)+\cos(\theta)\right) \\ \frac{D_{ut}\sqrt{3}}{36}\left(\sin\left(\theta+\frac{\pi}{3}\right)+\cos\left(\theta+\frac{\pi}{6}\right)\right) & \frac{D_{ut}\sqrt{3}}{36}\left(\sin(\theta)-\cos\left(\theta+\frac{\pi}{6}\right)\right) & \frac{D_{ut}\sqrt{3}}{36}\left(-\sin(\theta)-\sin\left(\theta+\frac{\pi}{3}\right)\right) \end{bmatrix} \cdot \begin{bmatrix} \varepsilon_1 \\ \varepsilon_2 \\ \varepsilon_3 \end{bmatrix} \quad (1)$$

2.1.2. Instrumentation

To enable measurement of the load distribution in the stud, the unthreaded section was instrumented with electrical resistance strain gauges (SGs) (Fig. 2e). In order to separate the contributions of axial and

where D_{ut} and A_{ut} denote the diameter and cross-sectional area of the unthreaded section, respectively, θ represents the angular position of SG_1 relative to the x' axis, and ε_i is the measured strain from the SG_i.

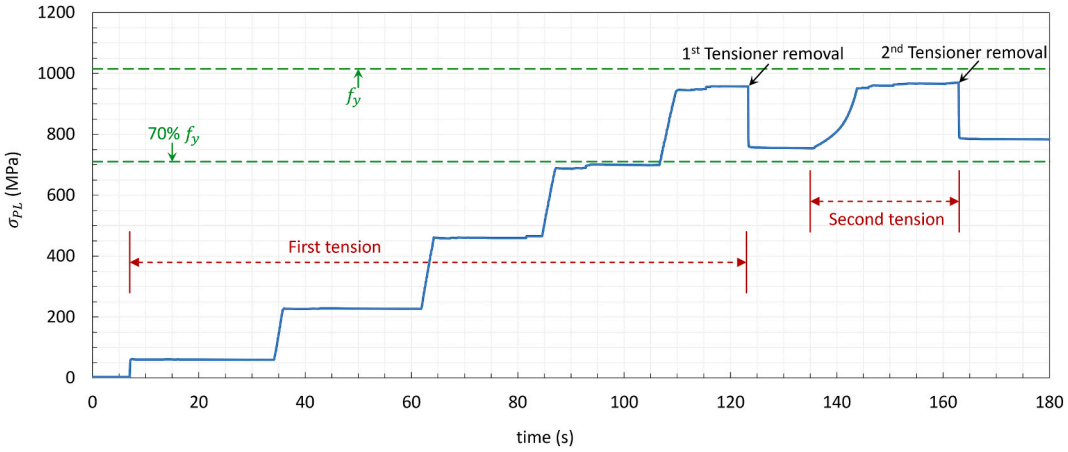

Fig. 3. Procedure of preload application (S12).

2.1.3. Application of preload

The studs were preloaded using a tension-tightening method, in which the preload is introduced in a torsion-free manner. In this procedure, the free end of the stud is gripped by an ITH hydraulic tensioner (Fig. 2b), which elongates the stud before the nut is tightened. The preload was applied in two tensioning stages, as illustrated in Fig. 3.

During the first tensioning stage, the hydraulic pressure was increased gradually in consecutive increments. This stepwise loading procedure was adopted to introduce the high preload in a controlled manner and to allow progressive seating of the contact interfaces between the stud, nut and flange. Such a gradual loading procedure for large-diameter studs loaded close to the yield strength, reduces the risk of abrupt load introduction, unstable settlement, or overshooting of the target preload. The hydraulic pressure was increased to a maximum value of 2000 bar, corresponding to a preload of approximately 1340 kN. This maximum pressure was intentionally selected to be higher than the desired residual preload because, upon release of the hydraulic pressure and removal of the tensioner, part of the applied preload is inevitably lost due to relaxation, local embedment of surface asperities and elastic spring-back effects.

Following the first tensioner removal, the stud was re-tensioned from 0 to 2000 bar in a single continuous loading step, followed by a second tensioner removal. The purpose of this re-tensioning procedure was to compensate for settlement effects that developed during the first tensioning cycle and thereby achieve a higher and more stable residual preload after the final tensioner removal.

The variation of the stud preload stress, $\sigma_{PL} = F_b/A_s$, during the entire preload application sequence is shown in Fig. 3. It can be observed that, at the end of the second tensioning stage, the stud preload reached approximately 95% of the yield strength. Following the final tensioner removal, the preload immediately decreased to about 79% of the yield strength due to elastic spring-back, local embedment, and settlement effects. As shown in Fig. 3, the residual preload after the second tensioner removal was approximately 5% higher than that obtained after the first. Nevertheless, the residual preload achieved after the second tensioning cycle was approximately 5% higher than that obtained after the first tensioner removal, demonstrating the effectiveness of the re-tensioning procedure in stabilising the clamping force. After preloading, fatigue testing was initiated 48-96 hours later to eliminate short-term relaxation effects.

The cyclic loading was applied using a 2 MN Instron uniaxial servo-hydraulic testing machine at Delft University of Technology. A constant amplitude cyclic load was applied to the shell section of the L-flange connection (Fig. 2a). During the first fatigue test, it was observed that the axial force in the stud remained almost unchanged when the external load was below 200 kN, owing to the high preload level in the connection (see Section 3.1). Consequently, for all subsequent tests, the minimum external load was maintained at 200 kN. This approach minimised unnecessary cyclic loading and potential fatigue damage in the L-flange components while having a negligible influence on the

Table 3
Applied loads and stress ranges in the studs for L-flange fatigue tests.

Stud	$F_{ext,max}$(kN)	$F_{ext,min}$(kN)	$F_{b,max}$(kN)	$F_{b,min}$(kN)	ΔM_b(kN.mm)	$\Delta\sigma_A$* (MPa)	$\Delta\sigma_B$** (MPa)	Nut-side failure
S01	549	50	1255	1115	412	95	52	Run-out
S01	609	200	1326	1109	573	148	72	top
S02	592	200	1311	1134	492	120	62	top
S03	592	200	1285	1093	546	131	69	bottom
S04	559	200	1255	1085	492	116	62	Run-out
S04	569	200	1268	1070	546	134	69	bottom
S05	574	200	1288	1109	501	122	63	bottom
S06	559	200	1253	1072	492	123	62	Run-out
S06	569	200	1263	1045	564	148	71	bottom
S07	599	200	1330	1142	500	128	63	top
S08	594	200	1342	1134	555	142	70	top
S09	574	200	1322	1132	519	129	65	top
S10	564	200	1304	1132	474	117	60	bottom
S11	559	200	1283	1115	474	115	60	Run-out
S11	564	200	1287	1093	519	132	65	top
S12	564	200	1303	1124	500	121	63	top

* Axial stress: $\Delta\sigma_A = \Delta F_b/A_s$.
** Bending stress: $\Delta\sigma_B = 4\sqrt{\pi}\Delta M_b/A_S^{1.5}$.

stress range experienced by the stud. The maximum external load was varied between tests to achieve fatigue lives within the high-cycle fatigue regime. The loading frequency was set to 1.5 Hz to avoid self-heating effects.

In total, 12 stud specimens were tested. The applied loads and the corresponding stress ranges in the studs are summarised in Table 3. After six tests, the L-flanges were replaced to avoid potential interaction effects or cumulative damage influencing subsequent tests. No visible fatigue cracks or permanent deformation were detected. Furthermore, all fatigue failures occurred in the studs, whereas the stress range in the flange remained below the fatigue strength corresponding to Detail Category 125 according to EC 3 [22], indicating an infinite fatigue life under the applied loading conditions. Consequently, cumulative flange damage and contact surface wear are considered negligible and are not expected to have influenced the measured fatigue behaviour of the studs in the subsequent tests.

Each test was continued up to 2×10^6 cycles, which is commonly considered the upper bound of high-cycle fatigue in steel structures. Specimens surviving this number of cycles without visible cracking were classified as run-outs. For the run-out specimens (S01, S04, S06, and S11), cyclic loading was continued beyond 2×10^6 cycles by increasing the external load without interrupting the test. Following failure, the fracture surfaces were carefully examined. No evidence of pre-existing cracks or beach marks associated with the preceding run-out stage was observed, indicating that the subsequent crack propagation and final failure were governed by the increased load level applied after 2×10^6 cycles.

2.2. Fatigue crack growth test

FCG experiments were conducted on eccentrically-loaded single edge crack tension (ESET) specimens according to ASTM E647 [51]. To obtain the FCG data, three ESET specimens were extracted from the threaded part of an M48 class 10.9 black stud with threads rolled after heat treatment, selected based on availability and supplied by the same manufacturer as the studs used in the L-flange fatigue tests (Fig. 4a). The notch was oriented perpendicular to the stud axis to ensure that the measured FCG behaviour was representative of cracks propagating normal to the stud axis, consistent with the crack orientation observed in the L-flange fatigue tests.

The tests were carried out using a servo-hydraulic fatigue testing machine. All experiments were conducted at F_{max}=6 kN and a high load ratio of $R = F_{min}/F_{max} = 0.7$, representing the high mean stress conditions present in preloaded studs. Crack growth was monitored using a crack gauge in combination with a crack opening displacement (COD) gauge (Fig. 4b). A FAC-20 crack gauge was bonded to the specimen, as shown in Fig. 4c. The gauge consists of grid lines spaced at 0.5 mm, which break sequentially as the crack advances, causing a measurable change in the output signal.

Before the main test, a fatigue pre-crack of 1 mm was introduced. The maximum load during precracking was set to 95% of the maximum load used in the main test. To expedite the precracking process, a lower load ratio of R=0.1 was employed.

The fatigue crack growth rate (FCGR) was determined using the Paris equation:

$$\frac{da}{dN} = C(\Delta K_I)^n \tag{2}$$

where C and n are material parameters, obtained from the FCG test. To determine the FCGR (da/dN), the incremental polynomial method with five consecutive data points [51] was employed. The mode I SIF range for the ESET specimens was calculated using the following expression from [51]:

$$\Delta K_I = \frac{\Delta F}{B\sqrt{W}} \cdot \frac{\sqrt{a/W}(1.4+a/W)}{(1-a/W)^{1.5}} \left[3.97 - 10.88(a/W) + 26.25(a/W)^2 - 38.9(a/W)^3 + 30.15(a/W)^4 - 9.27(a/W)^5\right] \tag{3}$$

where B and W are the specimen thickness and width, respectively. Fig. 5 shows the FCGR plotted against the SIF range on a log-log scale for the three ESET specimens. The results demonstrate that the FCG data from the different specimens exhibit very good consistency, confirming

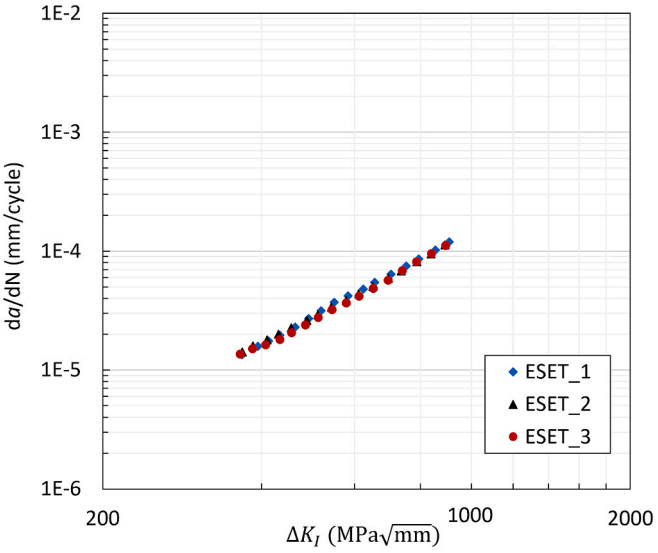

Fig. 5. FCGR as a function of SIF range for ESET specimens.

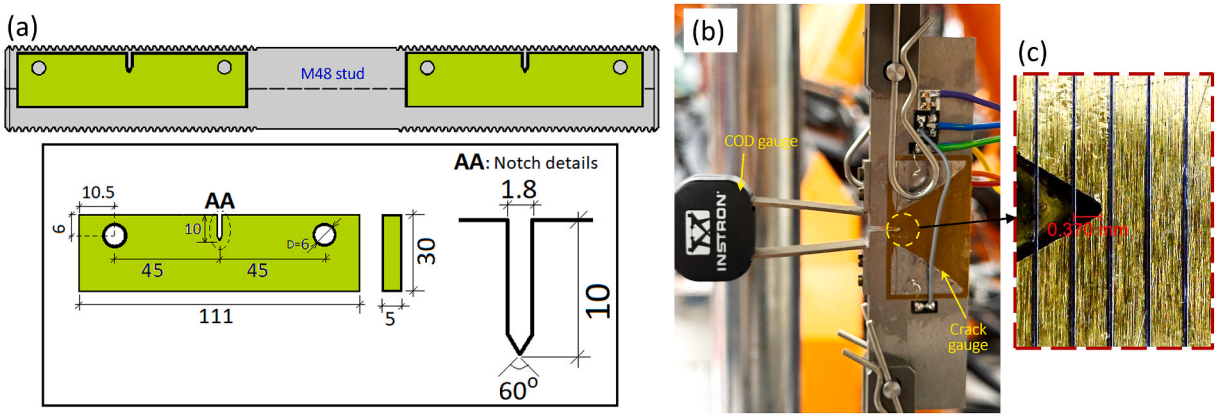

Fig. 4. (a) Specimens extracted from the M48 class 10.9 stud for FCG tests. (b) FCG test setup, (c) crack gauge used for crack length measurement.

Table 4
FCG parameters obtained from ESET specimen tests.

	n	C(mm & MPa)
ESET-1	2.415	8.5332×10^{-12}
ESET-2	2.277	19.9077×10^{-12}
ESET-3	2.450	6.2726×10^{-12}
Mean ± Stdv	2.381± 0.09	$11.571\times10^{-12} \pm 7.31\times10^{-12}$

the repeatability of the test procedure. It should be noted, however, that all specimens were extracted from the same stud. Therefore, although the obtained parameters are considered representative, some variability may exist between different studs, even within the same manufacturing batch.

The corresponding crack growth parameters derived from these tests are summarised in Table4. The material constants C and n were obtained by performing a linear regression of $\log(da/dN)$ versus $\log(\Delta K_I)$. The mean values of C and n were then used in the FCG simulations and subsequent fatigue life predictions.

2.3. Numerical model

2.3.1. Material assumptions

The tested L-flange connection was modelled using the commercially available FE software package ABAQUS [52], (Fig. 6). The M48 partially threaded stud and the corresponding ISR nut were modelled with detailed thread geometry (categorised as Model Class IV according to VDI 2230 Part 2 [53]). The stud thread was defined by a major diameter of D_{maj}=48.0 mm, a minor diameter of D_{min}=41.9 mm, and a thread-root radius of R_{th}=0.72 mm (Fig. 6c). The corresponding dimensions for the nut were D_{maj}=48.4 mm, D_{min}=42.6 mm, and R_{th}=0.36 mm, respectively. The stud includes an unthreaded section l_{ut}=112 mm long with a diameter of D_{ut}=45 mm, and the nut has an outer diameter of 92 mm.

A Young's modulus of E=210 GPa and a Poisson's ratio of ν=0.3 were used for all components. In addition, elastic-plastic material behaviour with isotropic hardening was employed for the flange, stud, and nut. The material properties assigned to the flanges, stud, and nut correspond to the values provided in Section 2.1.1. As the FE formulation requires true stress-strain data, the engineering stress-strain curves prior to necking were converted using the standard logarithmic relationships [52].

2.3.2. FE modelling of preload application

Due to the complexity of the model, a submodelling technique was employed. The global model of the L-flange connection was used to simulate the load transfer behaviour under preload and external loading. Fig. 7a illustrates the boundary conditions (BC) and loading applied to the global model. The bottom surface of the lower flange was fully constrained. The analysis was performed in two sequential steps:

- Step 1: Preloading phase. A temperature-field method was adopted to introduce the preload in the stud. A temperature reduction was applied exclusively to the stud, with a coefficient of thermal expansion of 1×10^{-5}, while all other parts were assigned zero expansion. Under these conditions, the thermal contraction of the stud is restrained by the nuts, resulting in a tensile force in the stud and a corresponding compressive load in the flange. Several temperature levels were examined to achieve the desired preload, and it was determined that a reduction of approximately 527 °C resulted in a

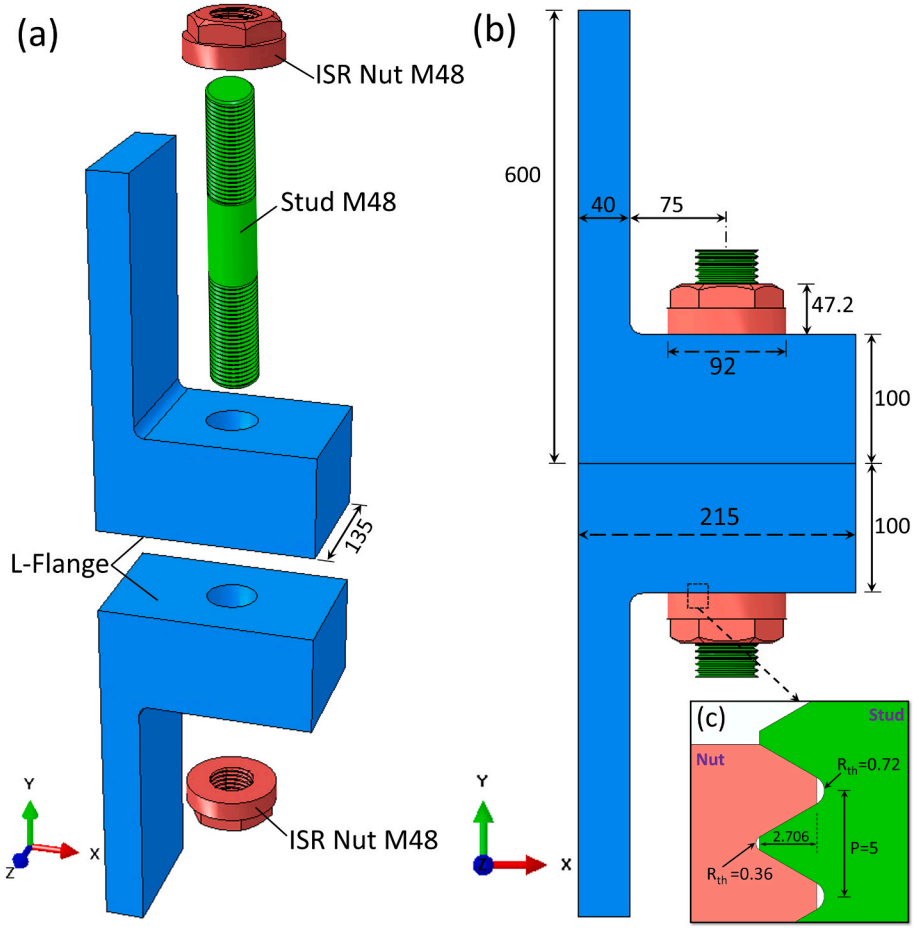

Fig. 6. (a) Exploded and (b) assembled representations of the L-flange connection incorporating an M48 stud and nut, (c) close-up of the thread geometry.

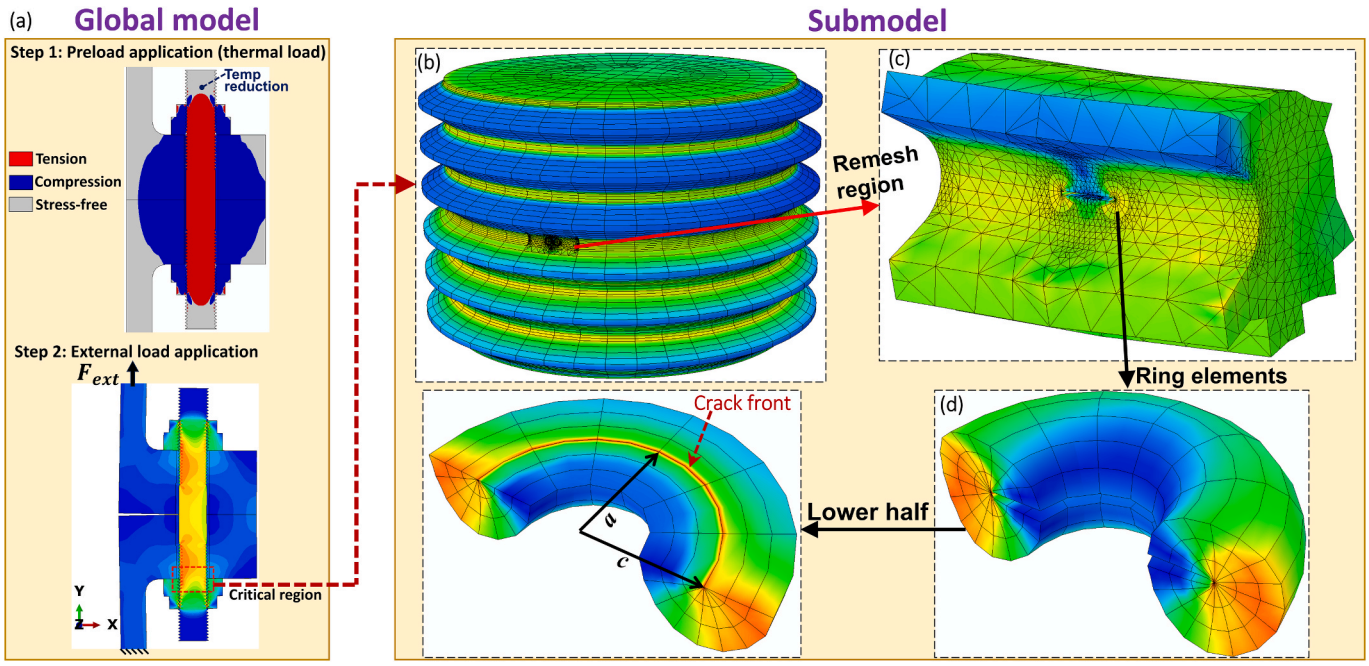

Fig. 7. Key aspects of the 3D FE modelling approach: (a) BCs applied to the global L-flange model during preload (Step 1) and external loading (Step 2) phases; (b) extracted submodel from the critical stud region; (c) semi-elliptical crack introduced at the thread root; (d) focused mesh refinement around the crack front using rings of quadratic hexahedral elements.

stud preload consistent with the experimental measurements as shown in section 3.1.

- Step 2: External loading phase. After establishing the target preload, the external load F_{ext} was applied to the top shell segment.

Contact interactions were defined using a general contact formulation for all relevant interfaces, including stud-nut threads, nut-flange contact, and flange-flange contact. Normal contact behaviour using a hard contact formulation was used, while tangential behaviour was modelled using a penalty-based friction law with a coefficient of friction of 0.2, representative of steel-on-steel threaded interfaces [54]. Previous parametric investigations [47,54] have demonstrated that reasonable variations in thread friction have a negligible effect on mode I SIF; therefore, the selected value was deemed sufficiently accurate.

All parts were discretised with 20-node quadratic hexahedral elements (C3D20R) using reduced integration and hourglass control to

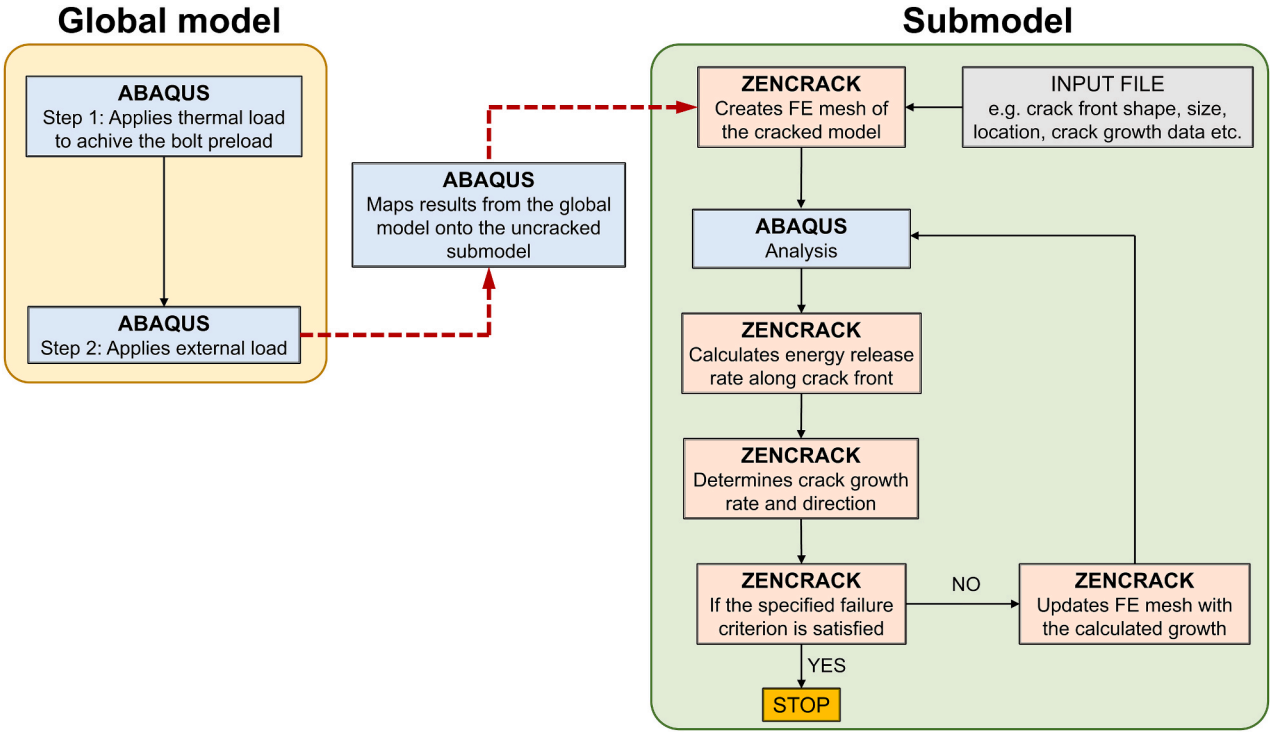

Fig. 8. Iterative workflow for three-dimensional FCG simulation using ABAQUS and ZENCRACK based on the submodelling and remeshing technique.

enhance computational efficiency. The simulations were conducted using an implicit solver with nonlinear geometry effects enabled, in order to capture contact nonlinearity and large deformation effects.

2.3.3. Fatigue crack growth simulation

Fatigue life assessment based on fracture mechanics was carried out through three-dimensional FCG simulations using ABAQUS 2023 [52] coupled with ZENCRACK 9.5-1 [55]. Given the high computational demand associated with the detailed geometry and nonlinear contact interactions, a global-local submodelling strategy was adopted. As shown in Fig. 7b, the submodel encompassed the first engaged thread between the stud and the lower nut, which is the critical region based on the maximum stress concentration observed in the global model and confirmed by experimental failure observations.

An initially uncracked submodel was first generated in ABAQUS. To ensure exact correspondence of nodal locations between the global and local models, the submodel was created by duplicating the global mesh and removing all regions outside the area of interest. BCs for the submodel were obtained by mapping the displacement fields from Step 2 of the global analysis onto the cut surfaces of the submodel.

The submodel was subsequently imported into ZENCRACK, where a semi-elliptical surface crack with an initial aspect ratio of $a_i/c_i = 1$ and an initial depth of $a_i = 0.5$ mm was introduced at the thread root, as illustrated in Fig. 7c. The overall workflow of the iterative 3D FCG analysis incorporating adaptive remeshing is presented in Fig. 8. An initial crack depth of a_i=0.5 mm was selected as a convenience value to compromise between physical representativeness and numerical stability. This crack size is small compared with the stud diameter, but sufficiently large to allow a well-defined crack front, stable remeshing and reliable SIF evaluation at the thread root. Moreover, an initial crack size of this order has previously been recommended and adopted in fracture-mechanics-based fatigue assessments of bolts [46,47] and offshore structures [56]. The initiation-propagation analysis presented later additionally shows that the experimentally observed change in bending response, used as an indication of crack initiation, is consistent with the formation of a crack of approximately this magnitude.

Crack propagation direction was determined based on the maximum energy release rate criterion. The energy release rate was evaluated at each node along the crack front, and crack advancement was governed by the node exhibiting the highest value [57]. The corresponding crack increment was then applied, and the crack front geometry was updated. As growth increments can vary along the crack front, its shape evolved during propagation. This process was repeated iteratively until the crack reached the average measured critical crack depth of a_c=11 mm, corresponding to approximately 26% of the minimum stud cross-sectional area and marking the onset of unstable crack growth. At this crack depth, the calculated maximum SIF was approximately 100 MPa$\sqrt{\text{m}}$, which is comparable to the estimated maximum SIF of 132 MPa$\sqrt{\text{m}}$ at the onset of fast fracture in the FCGR tests.

The uncracked submodel was initially meshed with 20-node quadratic hexahedral elements (C3D20R) using reduced integration. Afterward, a crack was introduced, and a region with a radius of 1.5 mm around the crack front was defined as the remeshing zone (Fig. 7c). Within this zone, the original elements were deleted, and wedge elements with a square-root singularity shape function were assigned along the crack front, arranged in a spider-web pattern (Fig. 7d). Three concentric rings of quadratic hexahedral elements (C3D20R) were employed around the crack tip to enable accurate J-integral calculations. The remaining part of the remeshing region was filled with quadratic tetrahedral elements (C3D10M). This remeshing procedure was repeated and updated as the crack propagated. Mesh refinement near the crack front was guided by a convergence study, which showed that a characteristic element size of 0.125 mm provided stable SIF results, with variations below 1% between successive refinements. The final submodel consisted of 32288 elements and 106207 nodes. Frictionless contact and hard normal behaviour were assigned to the crack faces. The analysis was performed using a modified Newton-Raphson scheme within the ABAQUS general static solver.

SIFs were extracted from the J-integral using the interaction integral method [52] as follows:

$$K_{\text{I}} = \frac{E}{2(1-\lambda\nu^2)} J_{\text{int}}^{\text{I}} \tag{4}$$

$$K_{\text{II}} = \frac{E}{2(1-\lambda\nu^2)} J_{\text{int}}^{\text{II}} \tag{5}$$

$$K_{\text{III}} = \frac{E}{2(1+\nu)} J_{\text{int}}^{\text{III}} \tag{6}$$

where J_{int} denotes the interaction integral, ν is the Poisson's ratio and λ=0 for plane stress or λ=1 for plane strain conditions. As the ratios $K_{\text{II}}/K_{\text{I}}$ and $K_{\text{III}}/K_{\text{I}}$ remained below 0.05 throughout the simulations, mode I fracture was dominant [58], and only K_{I} was considered in the fatigue life calculations.

3. Validation

The validation procedure adopted to assess the accuracy of the numerical models was carried out in two stages. First, the global FE model of the L-flange connection was assessed by comparing the numerically obtained LTF with corresponding experimental measurements, thereby confirming that the applied BCs and the preload implementation accurately represent the mechanical response of an ideal L-flange joint. Subsequently, the FCG framework was verified by benchmarking the predicted SIFs against reference solutions reported in the literature.

3.1. Validation of the preload modelling

In the first analysis step of the global FE model, a uniform temperature reduction of 527 °C was applied to the stud to generate a preload level matching the experimentally measured value for S01. In the subsequent step, an external tensile load of 550 kN was imposed on the segment specimen. Fig. 9 compares the experimentally measured response during cyclic loading with the FE predictions for the axial stud force (F_b) and the corresponding bending moment (M_b), evaluated at the same cross-section where the strain gauges were glued on the studs. Experimental observations indicate that both F_b and M_b remain nearly constant up to external loads of approximately 260 kN and 100 kN, respectively, after which a pronounced increase is observed with further loading. The numerical results closely reproduce this behaviour. These small deviations confirm the reliability of the adopted temperature-field method for modelling the bolt preload and demonstrate its feasibility for representing stabilised preload conditions in bolted flange connections.

It should be noted that the temperature-field method is employed solely as a numerical tool to generate the target preload and does not represent a physical thermal loading condition. The applied temperature reduction was calibrated to reproduce the experimentally measured preload level after tension-tightening. Moreover, the material properties were defined as temperature-independent; therefore, the applied temperature field only generated thermal strain and did not affect the material response in any other way. Consequently, the subsequent stress state is governed by the achieved preload rather than by the specific values of temperature reduction or thermal expansion coefficient used in the model. Different combinations of thermal expansion coefficient and temperature change that produce the same stud elongation result in essentially the same preload state and contact conditions after equilibrium is reached. Therefore, the temperature reduction should be regarded as a numerical parameter for preload generation rather than a physical variable affecting the fatigue assessment.

The temperature-field method was adopted because it provides a

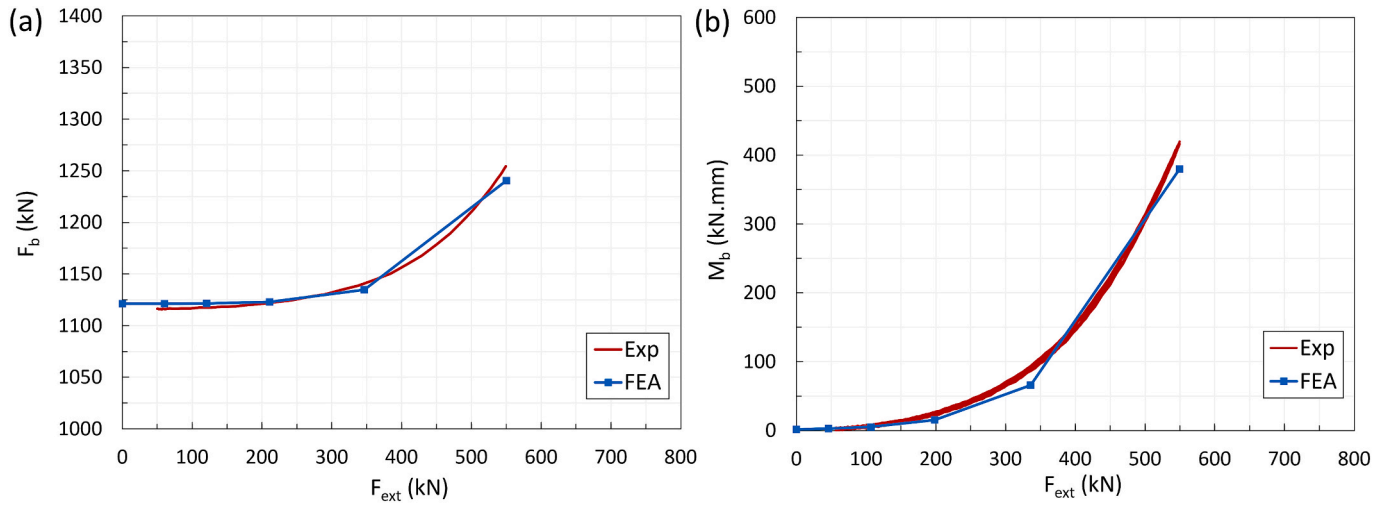

Fig. 9. Comparison of experimentally measured and numerically predicted (a) stud force F_b and (b) bending moment M_b as functions of the external load applied to the flange for S01.

robust and convenient means of introducing preload uniformly over the full stud length in a detailed threaded model with nonlinear contact interactions. Unlike pretension-section methods, this approach does not require the definition of an artificial pretension plane within the stud. This is particularly beneficial in the present study, where axial force and bending moments are validated using SGs glued on the unthreaded section of the stud. Although the required temperature reduction must be calibrated to achieve the target preload level, the approach is especially applicable to studs in a connection in which preload is introduced through axial elongation of the stud, particularly when detailed thread geometry and contact interactions are modelled.

3.2. *Verification of the fatigue crack growth simulation*

The accuracy of load and BCs transfer from the global model to the submodel was verified by comparing the resultant axial force and bending moment at the cross-section corresponding to the root of the first engaged thread. The discrepancies between the global and submodel results were up to 1.49% for force and 1.81% for moment, confirming reliable transmission of loads and BCs.

The three-dimensional FE-based FCG modelling framework was subsequently verified by comparison with published results from literature [59–61]. To ensure compatibility with available reference data, a benchmark model was constructed consisting of a semi-elliptical surface

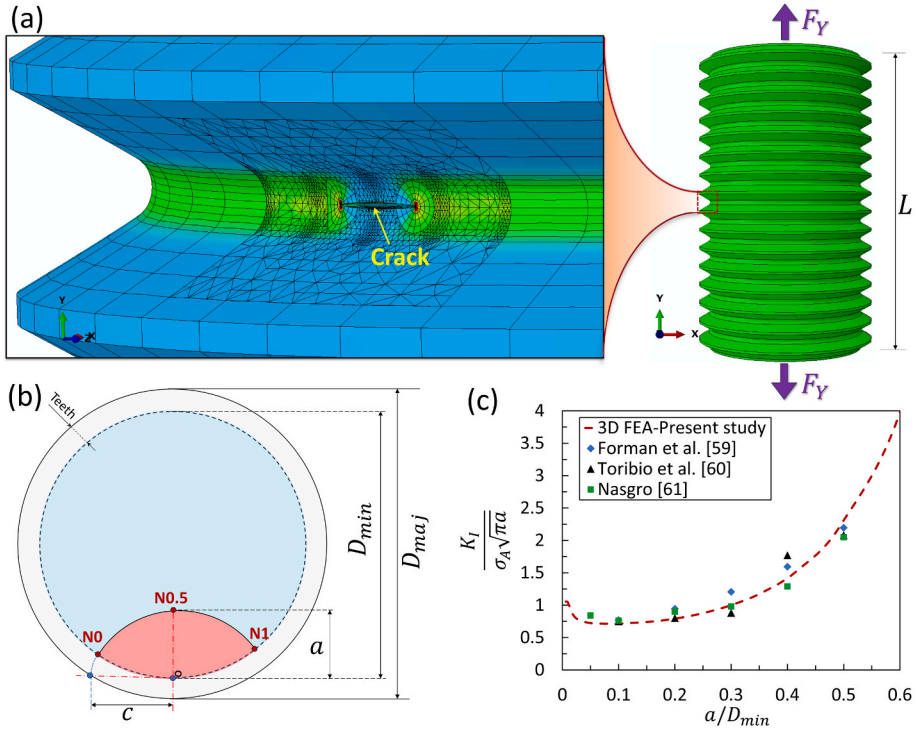

Fig. 10. (a) Geometry of the 3D axisymmetric M48 threaded rod used for model verification, showing a semi-elliptical crack located at the centre of the thread root and subjected to remotely applied axial loading. (b) Schematic representation of the crack geometry and node numbering at the thread root. (c) Comparison of dimensionless SIF values at the surface node (N1) along the crack front of a semi-elliptical crack under axial loading, obtained from the present study and Refs. [59–61].

crack in an M48 threaded rod without a nut, having a length-to-minor-diameter ratio of $L/D_{\min} = 1.65$. The thread was modelled as axisymmetric with a zero helix angle, and the rod was subjected to remotely applied pure axial loading F_Y=10 kN, as illustrated in Fig. 10a. The variation of the dimensionless SIF, based on $\sigma_A = 4F_Y/(\pi D_{min}^2)$, with normalised crack length for the surface node along the crack front (node N1 in Fig. 10b) is presented in Fig. 10c. The SIF values predicted by the present FE model exhibit close agreement with those reported in the literature. However, discrepancies are observed at larger crack sizes, which can be mainly attributed to the assumption of a fixed crack aspect ratio during crack propagation in the reference studies, whereas crack shape evolution is explicitly accounted for in the present analysis. In addition, part of the observed differences may be associated with variations in detailed thread geometry, such as the root radius and tooth height, which can locally affect the stress field.

4. Results and discussion

This section discusses the experimental observations and numerical results obtained from the fatigue tests and fracture-mechanics-based simulations. First, the evolution of preload relaxation before and during cyclic loading is analysed and its implications for load transfer and stress range in the stud are examined. The observed fracture mechanisms and failure locations are then correlated with stress distributions obtained from the FEA. Based on the measured axial and bending stresses, S-N curves are constructed using both effective and equivalent stress ranges, and the influence of bending and preload loss on fatigue life scatter is evaluated. The experimental results are subsequently compared with predictions from relevant standards for the sake of comparison. The fatigue life predicted by the numerical FCG framework is also compared with experimental data. The influences of crack-front evolution, initial crack geometry, and preload-induced overload effects on fatigue performance are discussed.

4.1. Loss of preload

Fig. 11a shows the time-dependent evolution of preload relaxation, the first 5 seconds after the hydraulic tensioner was released, and until the first two cycles. The results indicate that the most pronounced preload reduction takes place within the first 24 hours, after which the rate of relaxation gradually diminishes. This early-stage preload loss is mainly attributed to local flatening of surface asperities, plastic deformation at thread contacts, and micro-settlement effects in the clamped parts. Additionally, an immediate decrease in preload is observed at the initiation of cyclic loading, occurring within the first few load cycles. This behaviour is attributed to plastic shakedown under the applied mean stress, after which the material response stabilises and remains predominantly elastic due to shakedown effects [62]. An example of first two cycles of stud 12 (S12) is shown in Fig. 11b. The maximum axial stress during cyclic loading is 885 MPa, which is equal to 87% of the measured yield strength of 1014 MPa. This causes a drop in preload stress of only 5 MPa compared to the level just before applying cycling load. This shows that the "preload loss limit", which is defined as 85% of yield in IEC 61400-6 AMD1 [63] Eq. (29), is potentially conservative and improvements are possible.

While part of the preload loss stabilises after few load cycles, the

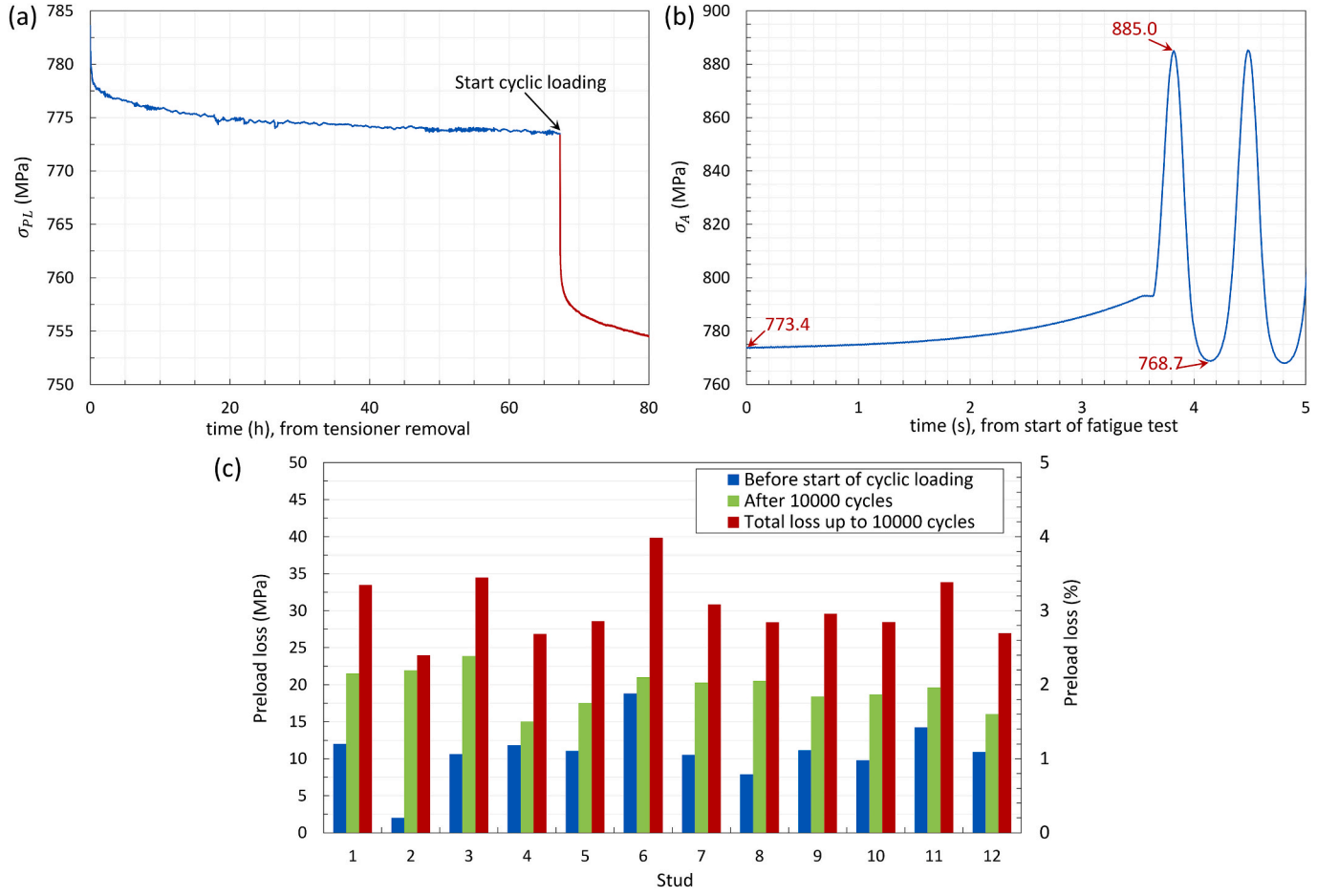

Fig. 11. (a) Preload relaxation after tensioner removal until cyclic loading for S12 (b) Axial stress in stud during first cycle of fatigue loading (c) Preload loss relative to the reference value after tensioner removal.

relaxation continues gradually over time. This has direct implications for fatigue assessment, since a reduced clamping force changes the load transfer mechanism function, increasing the stress range in the stud during cyclic loading. Fig. 11c presents the scatter in preload loss for different studs, taking the preload measured 5 seconds after tensioner removal as the reference, and comparing the values prior to the start of cyclic loading and after 10000 cycles. On average, the preload loss before the start of cyclic loading was 11 ± 3.9 MPa, while an additional loss of 9.6 ± 2.7 MPa occurred during the first 10 000 cycles, resulting in a total loss of approximately 30.4 ± 4.5 MPa. A noticeable increase in preload loss is observed once cyclic loading is applied, indicating that cyclic loading accelerates the relaxation process. It is hence favourable to re-tighten bolts after some time of operation, as loss of preload will converge to a stable value relatively fast, and the early losses can then be compensated. IEC 61400-6 AMD1 [63] (clause 6.7.3.2) provides detailed guidance regarding re-tightening and consideration of reduced losses depending on the tightening method. For instance, when tension-tightening is applied, re-tightening should be performed after a minimum of 240 power production hours and no later than six months after commissioning.

According to IEC 61400-6 [63], the total preload loss can be expressed as the sum of the losses due to settlement (embedment) and plastic strain development:

$$\Delta F_{loss} = \Delta F_Z + \Delta F_{pl} \tag{7}$$

where ΔF_Z is the preload loss caused by settlement of the contact surfaces and thread flanks, and ΔF_{pl} is the preload loss associated with plastic strain development in the joint components. The preload loss due to settlement can be estimated as

$$\Delta F_Z = \frac{f_Z}{\delta_s + \delta_p} \tag{8}$$

where f_Z is the total embedment, and δ_s and δ_p are the elastic resiliences of the stud and clamped parts, respectively. For the investigated connection, the elastic resiliences were calculated according to VDI 2230 Part 1 [64] as $\delta_s = 9.06 \times 10^{-7}$ mm/N for the stud and $\delta_p = 8.86 \times 10^{-8}$ mm/N for the clamped parts. The detailed calculations are presented in Appendix B. Seidel [5] recommended a total embedment value of $f_Z = 35\,\mu$m for uncoated flange connection. Using this value, together with the calculated elastic resiliences and a stud stress area of $A_s = 1470\,\text{mm}^2$, the corresponding preload loss due to settlement is estimated to be approximately 23.9 MPa.

The preload loss due to plastic strain development is estimated according to IEC 61400-6 [63] as:

$$\Delta F_{pl} = 0.05 F_{p,mean} \tag{9}$$

where $F_{p,mean}$ is the design preload force, calculated from:

$$F_{p,mean} = F_{p,inst,mean}\left(1 - 0.736 \times COV_p\right) \tag{10}$$

For the present tests, the mean preload force measured 5 second after tensioner removal was $F_{p,inst,mean}$=1152.9 kN, with a corresponding coefficient of variation of COV_p=0.0149. Using Eqs. (9) and (10), the preload loss associated with plastic strain development is estimated to be 38.8 MPa. Consequently, the total preload loss predicted by the IEC procedure is $\Delta\sigma_{loss}$=62.7 MPa.

In contrast, the most pronounced experimentally measured preload loss was approximately 40 MPa. A likely explanation for this difference is the preload application procedure employed in the present study, in which the studs were tensioned twice. During the first tensioning cycle, a substantial portion of the local surface settlement and asperity flattening at the bearing surfaces and thread flanks is expected to occur. Consequently, the remaining embedment during the second tensioning cycle and subsequent service loading is significantly reduced. Therefore, the preload loss predicted using the embedment value of $f_Z = 35\,\mu m$ is likely conservative for the present connection. In addition, Eq. (9), used to estimate the preload loss due to plastic strain development, was derived for joints subjected to relatively high operational loads, whereas the fatigue load applied in the present study is lower. Furthermore, the preload-loss recommendations in IEC 61400-6 were primarily developed for conventional HV bolted assemblies. The present connection differs through the use of hydraulic tension-tightening, ISR nuts, and a re-tensioning procedure, all of which contribute to a more stable residual preload. Therefore, a lower preload loss than that predicted by the standard procedures is physically reasonable and consistent with the experimental observations.

4.2. Fracture mechanism

Fig. 12 (a) shows the fracture surfaces of the investigated studs. In all tests, failure occurred in the first engaged thread between the stud and the nuts. The FE stress analysis of an L-flange model without a crack (Fig. 12b) shows that the maximum stress occurs at the first engaged threads between the stud and the upper and lower nuts on the shell side of the L-flange, which is subjected to maximum bending stress at the root. This maximum stress is evidently responsible for a crack initiation. In 58% of the cases, failure occurred at the upper nut, while in 42% it occurred at the lower nut (see Table 3).

Fractographic examination revealed the presence of ratchet marks on the fracture surfaces, indicating that fatigue cracking initiated from multiple microcracks at the thread root rather than from a single dominant defect. Owing to the severe stress concentration at the first engaged thread, several microcracks nucleate at neighbouring locations around the thread circumference. As these cracks propagate approximately perpendicular to the stud axis, they eventually merge to form a dominant crack front, leaving ratchet marks as visible boundaries between adjacent crack fronts (Fig. 12f).

As observed in Fig. 12c, three distinct regions can be identified on the fracture surfaces: a comparatively smooth and flat region corresponding to stable FCG, a rough transition region, and a rough inclined region associated with final unstable fracture.

Although the stud material exhibits ductile behaviour, fatigue cracks propagate with little deformation. Consequently, the stable FCG region remains approximately perpendicular to the direction of the maximum principal normal stress, similar to the orientation commonly observed in cleavage-type fracture surfaces. As crack propagation progresses and the remaining load-carrying cross-section decreases, the local stress level increases until unstable crack growth occurs. Due to the high preload applied to the stud, the mean stress level in the connection is elevated, resulting in a relatively smaller stable FCG region and an earlier transition to final unstable fracture. Since the differences between the applied stress ranges were relatively small, the critical crack depth corresponding to the onset of unstable crack growth (a_c) showed limited variation among the specimens (see Table 5). The average experimentally measured critical crack depth was a_c=11 mm, corresponding to approximately 26% of the minimum stud cross-sectional area at the thread root. This indicates that unstable crack growth was initiated after only a partial reduction in the load-carrying cross-section, primarily due to the high mean stress imposed by the preload.

The final unstable fracture region exhibits a rough and inclined surface morphology characteristic of ductile overload failure governed primarily by maximum shear stresses. Unlike the stable FCG region, this unstable fracture surface deviates from a plane perpendicular to the stud axis because significant plastic deformation develops immediately prior to failure.

4.3. S-N curve based on the effective stress (bending reduction factor)

Due to the eccentricity between the applied external load and the stud axis, a bending moment is induced in the stud, leading to a non-uniform stress distribution across the stud cross-section (Fig. 13a). If

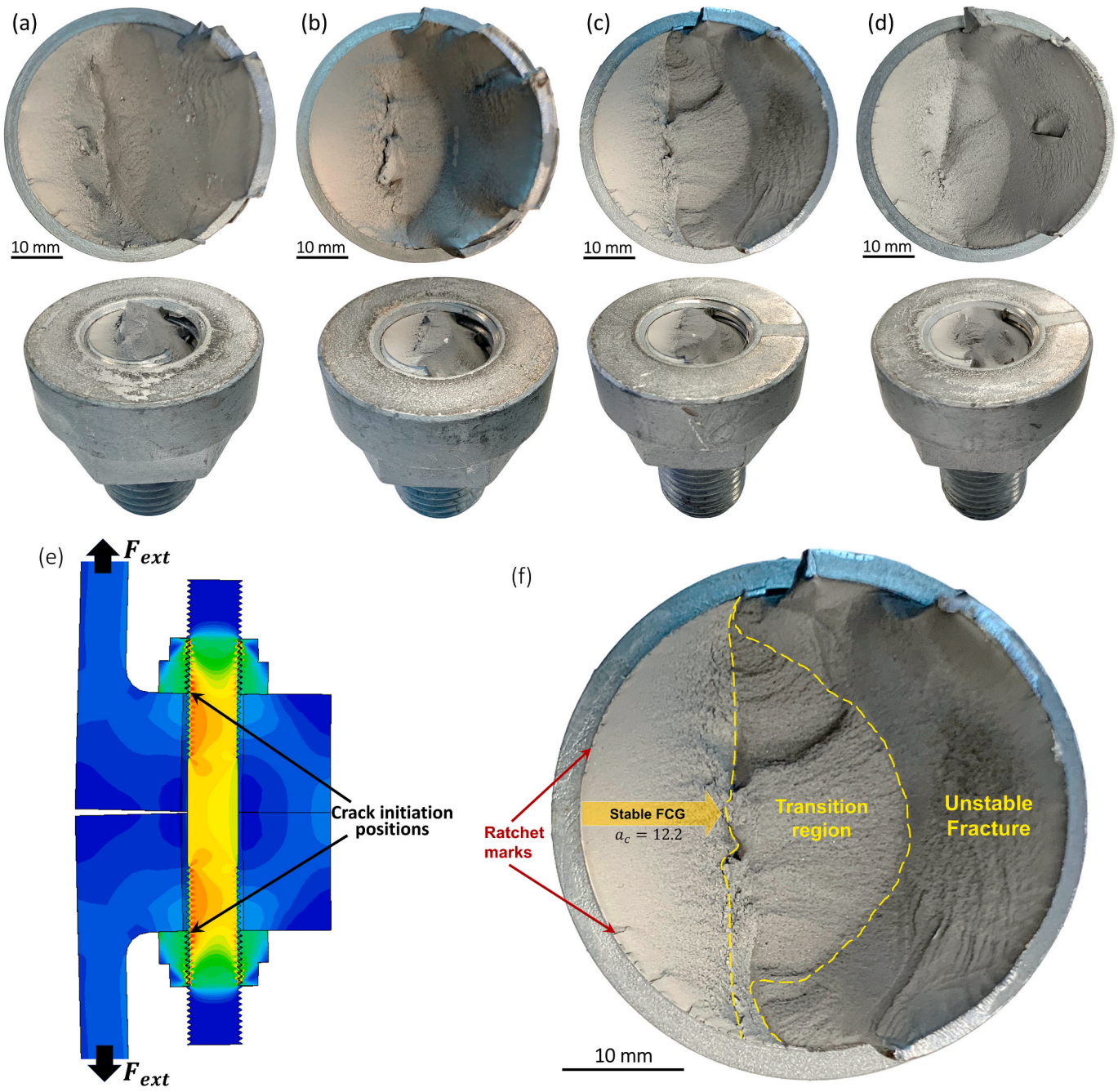

Fig. 12. Fracture surfaces of the investigated studs: (a) S03: $\Delta\sigma_A = 131$ MPa, $N_f = 145701$, (b) S04: $\Delta\sigma_A = 134$ MPa, $N_f = 295443$, (c) S07: $\Delta\sigma_A = 128$ MPa, $N_f = 222322$, and (d) S08: $\Delta\sigma_A = 142$ MPa, $N_f = 108493$. (e) Crack initiation positions based on the FE stress analysis (f) stable FCG, transition and unstable fracture regions for S07.

the maximum combined stress range ($\Delta\sigma_A + \Delta\sigma_B$) is directly used for fatigue evaluation as in case of axially loaded stud, the resulting S-N curve becomes overly conservative. This is because bending stresses are less damaging to fatigue life than axial stresses, due to the presence of stress gradients across the section [20]. To account for this difference in damage contribution, an effective stress range is defined as:

$$\Delta\sigma_{eff} = \Delta\sigma_A + k_b \times \Delta\sigma_B \tag{11}$$

where $\Delta\sigma_A$ and $\Delta\sigma_B$ represent the stress ranges due to pure axial force and bending moment, respectively. The bending reduction factor k_b is introduced to scale the bending stress component such that fatigue damage under combined axial-bending loading can be correlated with that under pure axial loading, as illustrated in Fig. 13b. This enables the use of conventional S-N curves, which are typically derived from pure axial fatigue tests, for the assessment of combined loading conditions.

In the present study, the k_b was determined using a fracture-mechanics-based approach. Two synthetic S-N curves were generated for an M48 threaded rod (Fig. 13c): one subjected to pure axial loading and the other to pure bending loading. For each loading condition, the number of cycles to failure was calculated over a range of stress levels using Eq. (2), assuming an initial crack depth of 0.5 mm and employing the mean FCG parameters listed in Table 4. The following SIF solutions for axial and bending loading were adopted in the calculations [65]:

Table 5
Loads and stress ranges for L-flange fatigue tests.

Stud	$\Delta\sigma_A$(MPa)	$\Delta\sigma_B$(MPa)	$\Delta\sigma_{eff}$(MPa)	$\Delta\sigma_{eq}$(MPa)	N_f(Exp)	a_c(mm)	N_{ini} Eq. (28)	N_{pro} Eq. (24)	N_f Eq. (29)	N_f error (%)
S01	148	72	191	194	123570	9.9	11508	109409	120917	−2
S02	120	62	157	162	447966	12.4	22221	164215	186437	−58
S03	131	69	172	180	145701	13.1	14981	126957	141938	−3
S04	134	69	175	176	295443	13.4	16216	133186	149402	−49
S05	122	63	160	161	853454	9.5	22707	166019	188727	−78
S06	148	71	191	191	122570	7.1	12399	115357	127756	4
S07	128	63	165	172	222322	12.2	18375	148025	166400	−25
S08	142	70	184	190	108493	10.8	12389	114441	126831	17
S09	129	65	168	175	222078	11.1	16903	138232	155135	−30
S10	117	60	153	160	220631	11.2	23227	169427	192654	−13
S11	132	65	171	171	413510	12.1	18360	146554	164914	−60
S12	121	63	159	167	174387	9.2	19947	152826	172773	−1

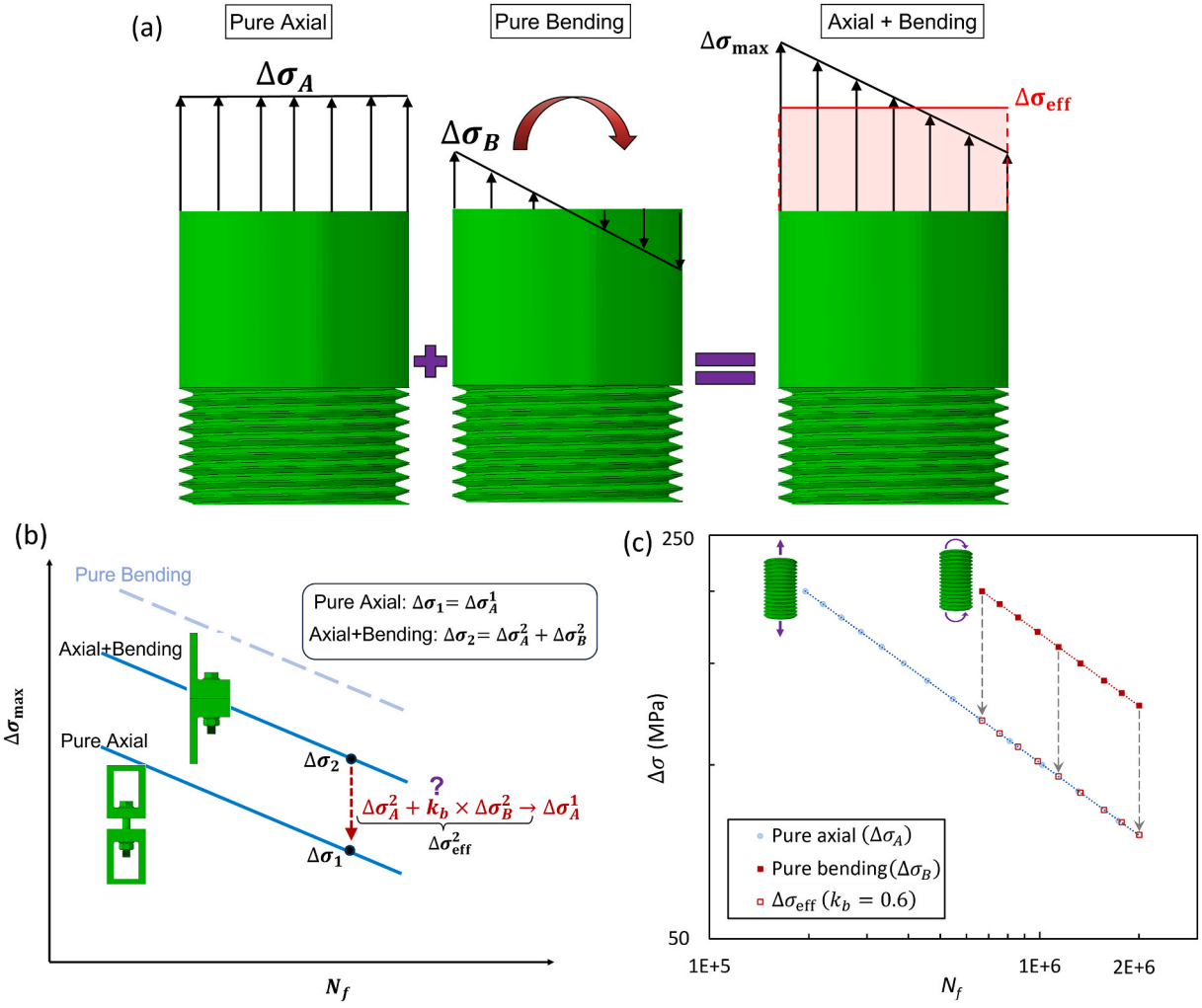

Fig. 13. (a) Non uniform stress distribution in the stud cross section due to axial and bending load (b) Using k_b to correlate S-N curve of axial-bending to pure axial loading (c) Synthetic S-N curves generated for pure axial and bending loads.

$$\Delta K_{I,A} = \Delta\sigma_A \left[2.043\exp\left(-31.332\left(\frac{a}{D_{min}}\right)\right) + 0.6507 + 0.5367\left(\frac{a}{D_{min}}\right) + 3.0469\left(\frac{a}{D_{min}}\right)^2 - 19.504\left(\frac{a}{D_{min}}\right)^3 + 45.647\left(\frac{a}{D_{min}}\right)^4 \right] \sqrt{\pi a} \quad (12)$$

$$\Delta K_{I,B} = \Delta\sigma_B \left[0.6301 + 0.03488\left(\frac{a}{D_{min}}\right) - 3.3365\left(\frac{a}{D_{min}}\right)^2 + 13.406\left(\frac{a}{D_{min}}\right)^3 - 6.0021\left(\frac{a}{D_{min}}\right)^4 \right] \sqrt{\pi a} \quad (13)$$

The fatigue life calculations were performed until the maximum SIF reached $K_{I,max} = 132$ MPa$\sqrt{\text{m}}$, corresponding to the onset of unstable fracture observed in the FCGR tests. For the pure bending case ($\Delta\sigma_A = 0$), the effective stress range is expressed as $\Delta\sigma_{\text{eff}} = k_b \times \Delta\sigma_B$. The k_b was then calibrated such that the S-N curve obtained under pure bending coincides with that of pure axial loading ($\Delta\sigma_B = 0$), as shown in Fig. 13c. Based on this procedure, a value of $k_b = 0.6$ was obtained.

For comparison, Stolle et al. [66] reported a k_b value of 0.625 based on fatigue tests on M48 class 10.9 bolts under pure bending. Furthermore, IEC 61400-6 AMD1 [18] provides an empirical expression for k_b as a function of bolt nominal diameter:

$$k_b = 0.5 + 0.5\frac{\log D_{nom} - \log 36}{\log 150 - \log 36} \quad (14)$$

For the M48 stud considered in this study, this equation yields $k_b \approx 0.6$. The close agreement between the present result and values reported in the literature confirms the validity of the proposed fracture-mechanics-based approach for determining k_b.

It should be noted that k_b was derived exclusively from FCG calculations, as fracture mechanics provides a direct measure of the crack driving force under simultaneous axial and bending action, thereby allowing the influence of stress gradients associated with bending to be quantified in a physically consistent manner. Although fatigue crack initiation contributes to the total fatigue life, the existing strain-life-based initiation models do not allow a direct separation of bending and axial contributions. Therefore, the fracture-mechanics framework was considered the most suitable basis for determining k_b.

4.4. S-N curve based on the equivalent stress

The effective stress range introduced earlier was initially evaluated at the beginning of each fatigue test. However, it was observed that the minimum stress in the stud gradually decreased during cyclic loading (Fig. 14b), primarily due to preload relaxation (Fig. 14c), which is more pronounced under high mean stress conditions. This reduction in clamping force leads to an increase in the nominal stress range acting in the stud (Fig. 14d).

It is seen that the most significant changes occur within the first 10000 cycles, after which the stress range stabilises. On average, an increase of approximately 10% in the effective stress range was observed within this interval. For example, in S12 the effective stress range rose from 139 MPa at the first cycle to 153 MPa after 10000 cycles. To capture this behaviour more accurately, the equivalent stress range is defined as the effective stress range at 10000 cycles, i.e. after the majority of preload loss has occurred. Table 5 presents the calculated stress ranges for all fatigue tests that resulted in failure.

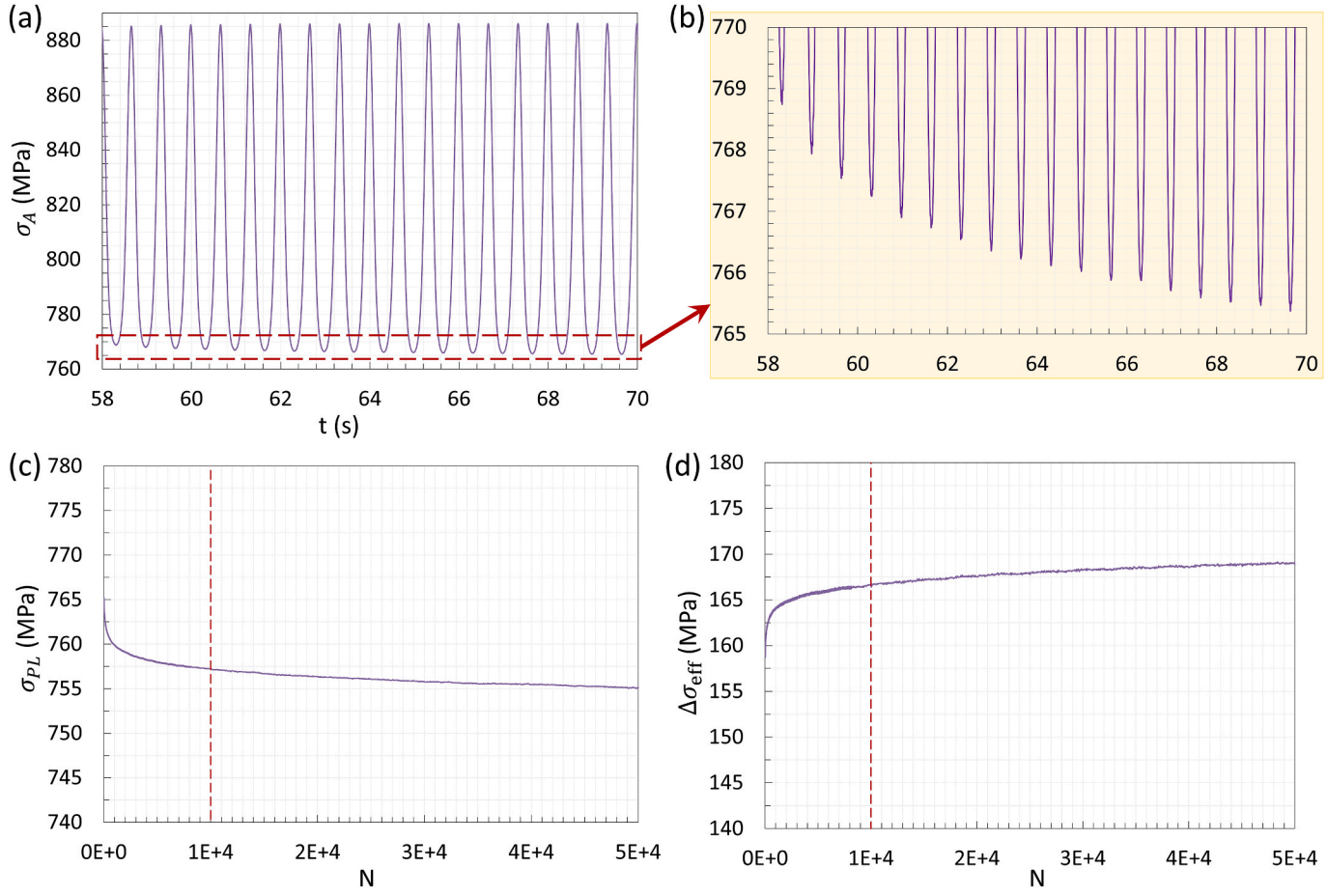

Fig. 14. (a) Cyclic load, (b) changes in minimum stress, (c) preload, and (d) stress range, during fatigue test for S12.

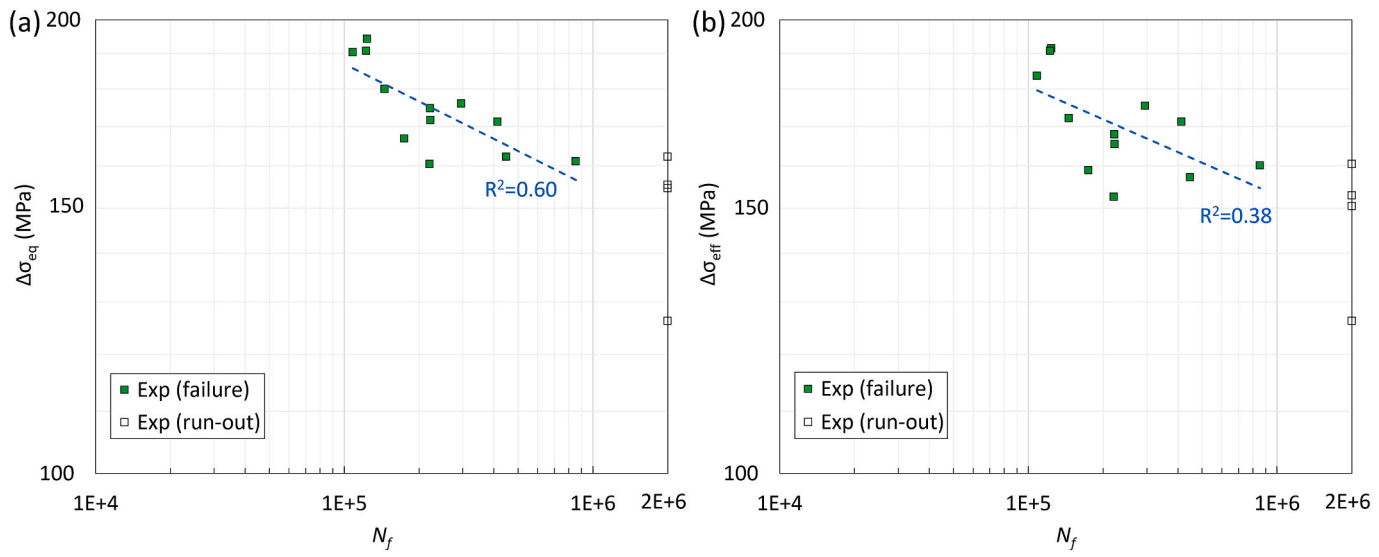

Fig. 15. S-N data based on the (a) effective stress range with k_b=0.6 (b) equivalent stress range corresponding to the effective stress range at 10000 cycles.

Fig. 15a and 15b present the resulting S-N curves based on the effective stress range at the first cycle and the defined equivalent stress range, respectively. Compared with the initial effective stress, the use of the equivalent stress range reduces the scatter of the fatigue data, demonstrating that it provides a more reliable and consistent fatigue damage parameter for eccentrically loaded flange connections under high bolt preload.

4.5. Fatigue life prediction based on the design standards

To evaluate the experimental results against existing design approaches, the predictions from EC3 [22], DNV [21] and IEC [18] were considered.

The S-N curve is expressed as a linear correlation between the number of cycles to failure (N_f) and the nominal stress range on a logarithmic scale, given by:

$$N_f = A(\Delta\sigma)^{-m} \tag{15}$$

where log$A$ and m denote the intercept and the inverse slope of the S-N curve, respectively, in the log-log representation. The parameter m is determined through linear regression of logN_f versus log$\Delta\sigma$, with the fatigue life treated as the dependent variable [67].

The mean S-N curves for these standards were obtained using the following formulation:

$$DC_{mean} = k_m \times k_s \times DC_{Table} \tag{16}$$

where DC_{Table} is the characteristic (design) detail category defined in the respective standard. The size factor k_s accounts for the influence of bolt diameter and is expressed as:

$$k_s = \left(\frac{D_{ref}}{D_{nom}}\right)^{\alpha_s} \tag{17}$$

Table 6
The mean detail categories for an M48 HDG bolt R-HT calculated based on different standards.

Standard	DC_{Table}	D_{ref}	α_s	m	t_l	DC_{mean}
EC3	50	30	0.25	3	1.9	56
DNV	63	25	0.25	3	2	69
IEC	63	30	0.1	3	2	77

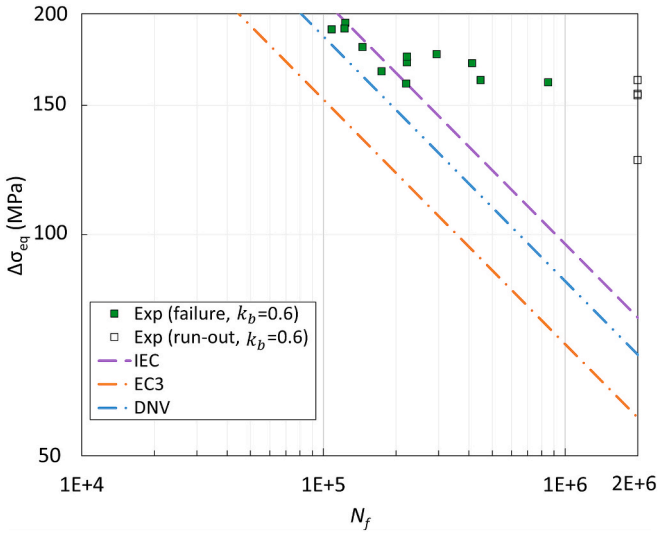

Fig. 16. Comparison of experimental data with the mean S-N curves predicted by various standards.

where D_{ref} is the reference diameter beyond which size effects become significant, D_{nom} is the nominal diameter and α_s is the size exponent. The factor k_m shifts the characteristic curve to estimate the mean S-N curve and is calculated as:

$$\log(k_m) = \frac{t_l \times \widehat{\sigma}_{\log N}}{m} \tag{18}$$

where t_l is the tolerance limit factor and $\widehat{\sigma}_{\log N}$ is the standard deviation of $\log(N_f)$ (commonly taken as 0.162 for high-strength steel [21]). DNV adopts a value of t_l corresponding to a 97.7% survival probability, whereas EC3 refers to a value corresponding to a 95% survival probability, see annex D of EN 1990 [68].

The calculated mean detail categories for an M48 HDG bolt rolled after heat treatment (R-HT) based on the standards are summarised in Table 6.

The resulting mean S-N curves, together with the experimental data, are presented in Fig. 16. The comparison shows that in the finite-life region (N $< 2\times10^5$ cycles), the IEC-based prediction provides good agreement with the experimental results, whereas the EC3 curve is

overly conservative. In addition, at the endurance limit (2×10^6 cycles), all standards predict considerably lower fatigue strength than observed in the experiments. The experimental endurance limit is markedly higher, suggesting that current design standards underestimate the long-life fatigue resistance of such connections.

This improvement in fatigue performance at long lives may be attributed to the preload application method. In this study, a tension-tightening (torsion-free) method was employed, in which the studs were temporarily subjected to overload levels during hydraulic tensioning. Previous studies [69–71] have demonstrated that overloading can retard fatigue crack growth through local plastic deformation and the associated residual stress redistribution. A similar mechanism is assumed to contribute to the enhanced fatigue performance observed in the present study. Although a macroscopic crack is not present at the time of preloading, micro cracks and microstructural defects may already exist in the hot-dip galvanised coating and coating-substrate interface [54,72]. In addition, the thread root itself acts as a severe stress concentrator. The high preload applied during tension-tightening may induce local plastic deformation at the thread root. Upon partial unloading during tensioner removal, the plastically deformed region is constrained by the surrounding elastic material, leading to the development of a beneficial compressive residual stress field analogous to that associated with classical overload-retardation mechanisms. Such a compressive residual stress field may increase the resistance to microcrack nucleation and early short-crack growth before a dominant fatigue crack is formed, thereby extending fatigue resistance. The effect is particularly pronounced at low stress ranges near the endurance limit, where the ratio of overload to constant-amplitude load is relatively high.

Therefore, the discrepancy between standard predictions and experimental results highlights the necessity to consider overload-induced effects when assessing fatigue of high-strength bolts/studs in wind turbine tower connections preloaded using tension-tightening method. While current codes provide conservative design curves, they may underestimate the actual endurance limit, potentially leading to over-designed and uneconomical solutions at infinite life range.

4.6. Fatigue life prediction based on the numerical analysis

The total fatigue life of the studs consists of fatigue crack initiation life (N_{ini}) and fatigue crack propagation life (N_{pro}). This section presents a fracture-mechanics-based approach for predicting N_{pro} together with a strain-based method for estimating N_{ini}, and examines their relative contributions to the fatigue behaviour of highly preloaded studs under combined axial and bending loading.

4.6.1. Fatigue crack propagation life

To determine the FCG life, the FE fracture mechanics simulations described in Section 2.4 were performed for all tests that resulted in failure. The corresponding crack propagation life was calculated based on the mode I SIF, expressed as:

$$K_I = (\sigma_A Y_A + \sigma_B Y_B)\sqrt{\pi a} \tag{19}$$

where σ_A and σ_B represent stresses due to pure axial force and bending moment, respectively, and are calculated as follows:

$$\sigma_A = \frac{4F_Y}{\pi D_{min}^2} \tag{20}$$

$$\sigma_B = \frac{32M_Z}{\pi D_{min}^3} \tag{21}$$

where F_Y and M_Z are axial force along the Y-axis and the bending moment around Z-axis at the crack plane location, respectively. The geometry factors for axial and bending loading, Y_A and Y_B, also referred to as dimensionless SIFs, were determined for the deepest node (node N0.5 in Fig. 17) along the crack front as follows:

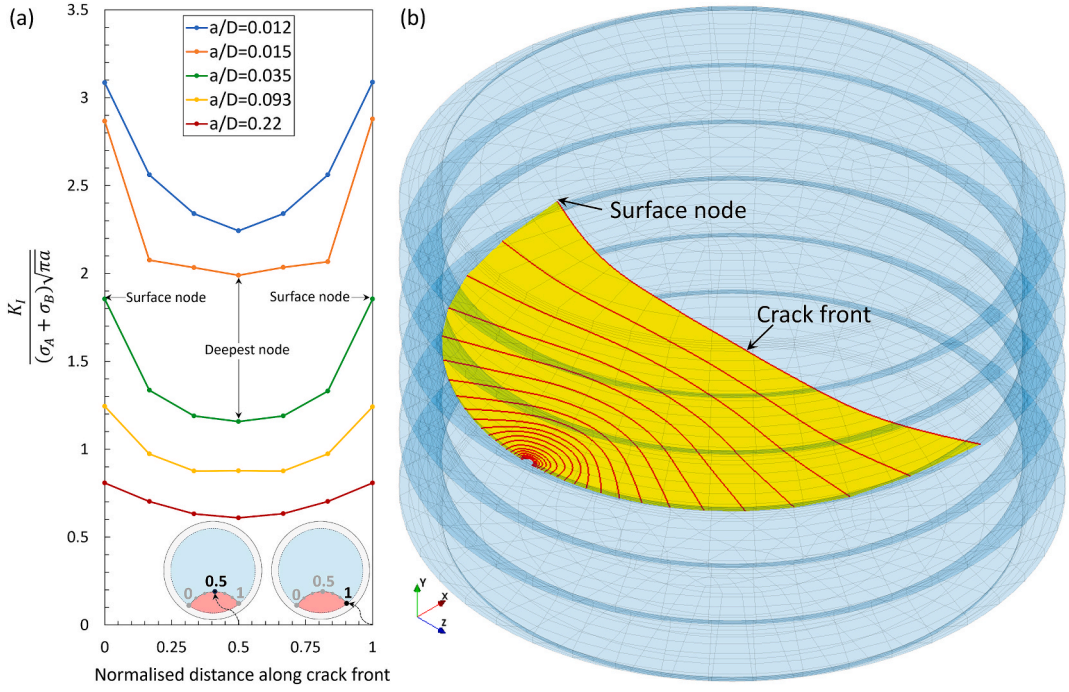

Fig. 17. Variation of dimensionless SIF along the crack front at different crack growth stages. (b) crack front profile evolution.

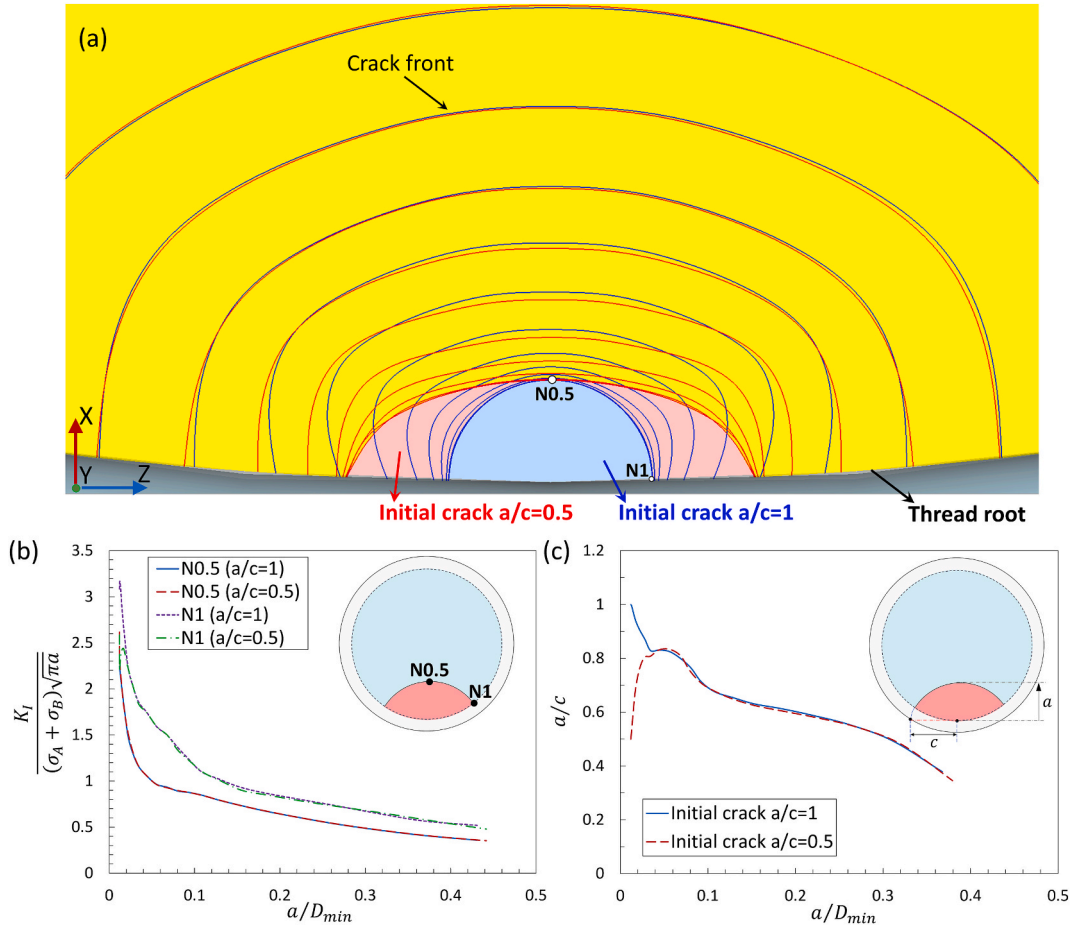

Fig. 18. Comparison of (a) evolution of the crack front profiles, (b) dimensionless SIF at deepest (N0.5) and surface (N1) nodes, (c) aspect ratio variation, for two initial cracks a/c=0.5 and a/c=1.

$$Y_A = \frac{0.2677\left(\frac{a}{D_{min}}\right)^2 - 0.003188\left(\frac{a}{D_{min}}\right) + 0.00005201}{\left(\frac{a}{D_{min}}\right)^3 + 0.266\left(\frac{a}{D_{min}}\right)^2 - 0.004755\left(\frac{a}{D_{min}}\right) + 0.00005516}, \quad 0.01 \leq a \Big/ D_{min} \leq 0.36 \tag{22}$$

$$Y_B = \frac{0.2055\left(\frac{a}{D_{min}}\right)^2 - 0.01347\left(\frac{a}{D_{min}}\right) + 0.0003594}{\left(\frac{a}{D_{min}}\right)^3 - 0.0528\left(\frac{a}{D_{min}}\right)^2 + 0.002972\left(\frac{a}{D_{min}}\right) + 0.000006373}, \quad 0.01 \leq a \Big/ D_{min} \leq 0.36 \tag{23}$$

The SIF solutions given in Eqs. (22) and (23) account for the transition of the crack front from a semi-elliptical to a nearly straight profile, assuming an initial crack aspect ratio of $a/c=1$ and an initial crack depth of $a = 0.5mm$.

Fig. 17a shows the variation of the dimensionless SIF along the crack front at different stages of crack growth. It is evident that the SIF values at the surface nodes is higher than at the middle nodes due to localised stress concentration at the thread root. This leads to faster crack propagation at the surface, driving the transformation of the crack front from a semi-elliptical to a nearly straight profile. Fig. 17b illustrates this evolution, showing how the initially semicircular front gradually transitions into an elliptical shape and eventually straightens as crack growth proceeds.

To examine the influence of the initial crack aspect ratio (a/c) on the SIF and crack front evolution, an additional simulation was performed for an initial semi-elliptical crack with $a/c = 0.5$ and $a = 0.5mm$. Fig. 18 compares the evolution of the crack front profile, the variation of the dimensionless SIF, and the change in aspect ratio as a function of crack length for the two initial crack geometries. It can be observed that after only a few crack growth increments, the crack with an initial $a/c = 0.5$ evolves toward a geometry similar to that of the initial $a/c = 1$ case. Beyond this stage, both the dimensionless SIF distribution and the crack front shape become practically identical, indicating that the effect of the initial crack aspect ratio diminishes as crack growth progresses.

The crack propagation life was calculated by numerically integrating the crack growth rate equation (Eq. (2)) using the trapezoidal rule with uniform crack length increments as follows:

$$N_{pro} = \int_{a_i}^{a_c} \frac{1}{C(\Delta\sigma_A Y_A + \Delta\sigma_B Y_B)^n (\pi a)^{n/2}} da \approx \frac{a_c - a_i}{2\pi^{n/2} kC} \sum_{j=i+1}^{k} \left(\frac{(a_{j-1})^{-n/2}}{\left[\Delta\sigma_A Y_A^{(a_{j-1})} + \Delta\sigma_B Y_B^{(a_{j-1})}\right]^n} + \frac{(a_j)^{-n/2}}{\left[\Delta\sigma_A Y_A^{(a_j)} + \Delta\sigma_B Y_B^{(a_j)}\right]^n} \right) \quad (24)$$

where a_i and a_c are the initial and critical crack sizes and k is the number of integration increments. The critical crack size adopted in the calculations was 11 mm, as discussed in Section 2.3.3.

4.6.2. Fatigue crack initiation life

To obtain the total fatigue life, the fatigue crack initiation (FCI) life should also be estimated. In the present study, the notch-strain approach examined by Eichstädt [73] for bolted assemblies and later calibrated by Wegener et al. [40] for M56 HDG class 10.9 bolts was adopted. The approach is based on the strain-life concept, in which the local strain response at the thread root is related to fatigue life through the Coffin-Manson equation:

$$\frac{\Delta\varepsilon_{loc}}{2} = \frac{\sigma_f'}{E}(2N_f)^b + \varepsilon_f'(2N_f)^{c'} \quad (25)$$

where σ_f', b, ε_f', and c' are the fatigue strength coefficient, fatigue strength exponent, fatigue ductility coefficient, and fatigue ductility exponent, respectively.

Since the strain-life curve is generally derived for fully reversed loading conditions (R= -1), mean stress effects must be incorporated separately for highly preloaded bolts subjected to tensile mean stresses. For this purpose, Eichstädt [73] recommended the use of the P_J damage parameter proposed by Vormwald [74], which is based on fracture-mechanical considerations of microscopic crack opening and closure. The P_J damage parameter is expressed as [74]:

$$P_J = 1.24\frac{(\Delta\sigma_{loc,eff})^2}{E} + \frac{1.02}{\sqrt{n'}}\Delta\sigma_{loc,eff}.\Delta\varepsilon_{p,loc,eff} \quad (26)$$

where n' is the cyclic strain-hardening exponent. The local stresses and strains are obtained from the cyclic stress-strain response at the root of the first engaged thread. For highly preloaded bolts, the stabilised cyclic loading condition remains predominantly tension-tension, and the minimum stress remains above the crack opening stress, therefore, the effective local stress range can be calculated as $\Delta\sigma_{loc,eff} = \sigma_{loc,max} - \sigma_{loc,min}$. The FCI life is then obtained by comparing the calculated P_J value with the corresponding P_J-life curve derived from the strain-life curve using the iterative procedure proposed by Haibach [75].

Hot-dip galvanised bolts exhibit reduced fatigue resistance due to shrinkage cracks present in the zinc coating, which introduce local microstructural stress concentrations [72]. To account for this effect, Eichstädt [73] proposed a strain amplification factor of S_f = 1.3, applied to the local strain range.

Using the abovementioned procedure and material parameters listed in Table 7, Wegener et al. [40] derived the following FCI curve for HDG M56 class 10.9 bolts:

Table 7
Material data used for calculating P_J parameter for M56 HDG bolt [40].

E(GPa)	f_u(MPa)	n'	σ_f'(MPa)	b	ε_f'	c'
216	1107	0.15	1661	−0.087	0.433	-0.58

$$N_{ini}^{(M56,HDG)} = 6.52 \times 10^{12}(\Delta\sigma)^{-3.74} \quad (27)$$

Since the present study employs the same bolt material class (HDG class 10.9), this relationship was adopted as the basis for estimating the crack initiation life of the M48 studs. To account for the difference in diameter between M56 and M48, a size-effect correction was applied using Eq. (17) together with the IEC parameters listed in Table 6. The resulting initiation-life relationship for the M48 HDG stud is:

$$N_{ini}^{(M48,HDG)} = 6.91 \times 10^{12}(\Delta\sigma_{max})^{-3.74} \quad (28)$$

where $\Delta\sigma_{max}$ is the maximum tensile stress range in the stud cross-section $\Delta\sigma_{max} = \Delta\sigma_A + \Delta\sigma_B$, as shown in Fig. 13a. The maximum stress range was used for the N_{ini} calculations because FCI is a highly localised phenomenon governed by the stress conditions at the most highly stressed location. Under combined axial and bending loading, the highest stress range occurs on the shell side of the stud (see Fig. 13a). Since fatigue cracks initiate at the thread root located in this critical side (see Fig. 12e), the maximum stress range provides a more representative parameter for crack initiation than the effective stress range, which was introduced to account for the reduced fatigue damage associated with bending in crack propagation and total-life assessments.

To further examine the validity of the predicted crack initiation life, the experimental fatigue test results from the L-flange specimens were analysed. Since fatigue crack initiation cannot be directly observed during testing, the maximum bending stress, $\sigma_{B,max}$, measured by the SGs was monitored as an indirect indicator of crack formation. The bending component was selected rather than the axial component because it was found to be more sensitive to the local stiffness reduction caused by crack formation at the thread root than the axial response. Furthermore, the maximum bending stress within the loading cycle was considered, since the crack is expected to be fully open at the maximum load level and therefore has the greatest influence on the measured stiffness. A reduction of 0.2% in $\sigma_{B,max}$ was adopted as the crack initiation criterion, as illustrated in Fig. 19a. This threshold was selected to be sufficiently larger than the measurement noise while still representing an early stage of damage development. The observed change is interpreted as the point at which a developing crack begins to affect the local stiffness of the stud cross-section.

Fig. 19b compares the experimentally determined crack initiation lives with the initiation curve given by Eq. (28). The experimentally observed initiation lives are generally longer than the predicted values, particularly in the endurance-limit region. It should be noted that the crack initiation relationship in Eq. (28), adopted from the literature, was originally derived for HDG bolts with threads rolled before heat treatment, whereas the studs investigated in the present study were manufactured with threads R-HT. This manufacturing process generally results in higher retained compressive residual stresses at the thread root after the final manufacturing stage and may therefore increase the crack initiation life. Furthermore, differences in thread tolerances and nut geometry may influence the local stress-strain response and, consequently, the fatigue crack initiation behaviour. The longer initiation lives observed experimentally, particularly near the endurance limit, may also be partly attributed to the initial overload introduced during the tension-tightening process. As discussed in Section 4.5, such an overload may increase the threshold SIF and retard microcrack formation and their integration into dominant crack formation at the thread root through the generation of compressive residual stresses. Previous studies [76–78] have likewise reported that overloads can significantly increase the threshold SIF and extend crack initiation time, or even suppress crack propagation entirely, due to the compressive residual stresses generated around the crack tip. These manufacturing- and preload-related effects were not explicitly considered in the present calculations. Therefore, the predicted number of cycles to crack initiation is an engineering estimate.

The ratio of the experimentally determined crack initiation life (N_{ini})

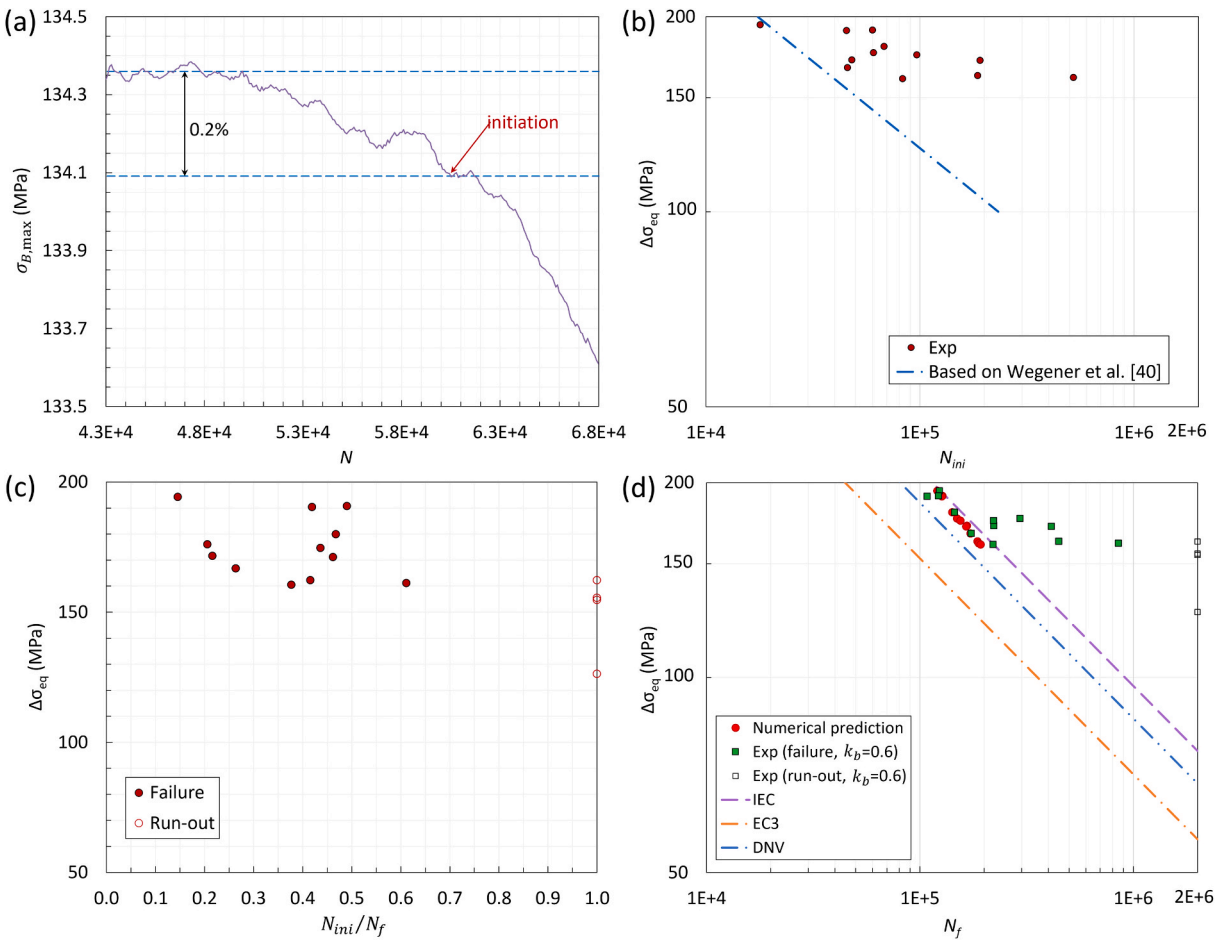

Fig. 19. (a) Illustration of the 0.2% change in bending stress used as an indicator of crack initiation; (b) equivalent stress range as a function of crack initiation cycles; (c) ratio of crack initiation life to total fatigue life for different equivalent stress ranges; (d) comparison of numerically predicted total fatigue life with experiments and design standards.

to total fatigue life (N_f) is presented in Fig. 19c for different equivalent stress ranges. The results show that approximately 20-50% of the total fatigue life is consumed during the crack initiation stage, indicating that crack propagation constitutes a significant portion of the total fatigue life in highly preloaded HDG studs subjected to combined axial and bending loading within the range of $\Delta\sigma_{eq} = 160 - 200$ MPa. A sensitivity assessment showed that increasing the threshold from 0.2% to 0.5% changes the estimated N_{ini}/N_f by only about 5%.

4.6.3. Total fatigue life

The total fatigue life is calculated as:

$$N_f = N_{ini} + N_{pro} \tag{29}$$

where N_{ini} and N_{pro} are obtained from Eqs. (28) and (24), respectively.

The predicted total fatigue lives are compared with the experimental data and design standard curves in Fig. 19d. The numerical predictions show very good agreement with the IEC S-N curve, as well as with the experimental results in the finite-life region ($N < 2 \times 10^5$ cycles). However, noticeable deviations are observed near the endurance limit, where overload-induced crack retardation effects become increasingly significant. The good agreement between the predicted and experimentally derived propagation lives further supports the assumption of an initial crack depth of a=0.5 mm adopted in the fracture-mechanics analysis. Moreover, the experimentally observed 0.2% reduction in bending stress appears to correspond approximately to the formation of a crack of similar size, providing additional justification for the selected initial crack depth.

5. Conclusions

This study investigated the fatigue life of an M48 class 10.9 HDG L-flange connection subjected to a high preload. Fatigue tests were first performed to quantify the influence of bending induced by load eccentricity on the fatigue behaviour. Subsequently, a comprehensive three-dimensional fracture-mechanics-based FCG analysis was performed to predict the crack propagation life. By combining the FCG analysis with a strain-based estimation of crack initiation life, a framework for predicting the total fatigue life of preloaded connections was proposed. Bolt preload was introduced using a thermo-mechanical FE procedure, and the model was validated against experimental results. Material parameters required for the numerical predictions were determined from FCG tests on specimens extracted from the stud material.

The key findings of this work are summarised as follows:

- Experimental results show that applying a high bolt preload using tension-tightening significantly improves the fatigue resistance, particularly in the fatigue-limit region. It was shown that existing standards provide overly conservative fatigue life estimates in the endurance-limit region for studs preloaded by tension-tightening.
- Preload relaxation during cyclic loading leads to an increase in the nominal stress range acting in the stud. The most significant changes occur within the first 10,000 cycles, after which the stress range stabilises. An average increase of approximately 10% in the effective stress range was observed. The experimentally measured preload loss corresponds to approximately 55% of the value predicted by the IEC

procedure, indicating that the standard approach is conservative for the investigated connection configuration.

- To account for the reduced damage induced by bending, an effective stress range was introduced. Furthermore, to incorporate preload loss due to cyclic loading, an equivalent stress range corresponding to 10,000 cycles was defined. This parameter significantly reduced the scatter in the fatigue data, demonstrating that it provides a more reliable and consistent fatigue-damage descriptor for eccentrically loaded flange connections under high preload.
- The effect of initial crack aspect ratio on the SIF and crack-front evolution was assessed. After only a few crack-growth increments, a crack starting from a/c=0.5 evolved toward a geometry similar to that of a/c=1. Beyond this stage, both the dimensionless SIF distribution and crack-front shape became effectively identical, indicating that the influence of the initial aspect ratio diminishes as crack growth progresses.
- The study demonstrated that bolt preload can be effectively induced in the FE model using a thermo-mechanical approach. SIF solutions for combined bending and axial loading were derived, and the fracture-mechanics-based framework successfully predicted S-N curves for preloaded bolted connections.

CRediT authorship contribution statement

Iman Shakeri: Writing – original draft, Visualization, Validation, Software, Methodology, Investigation, Formal analysis, Conceptualization. **Marc Seidel:** Writing – review & editing, Methodology, Formal analysis, Conceptualization. **Trayana Tankova:** Writing – review & editing, Supervision, Methodology, Conceptualization. **Milan Veljkovic:** Writing – review & editing, Supervision, Resources, Project administration, Methodology, Funding acquisition, Conceptualization.

Declaration of competing interest

The authors declare that they have no known competing financial interests or personal relationships that could have appeared to influence the work reported in this paper.

Acknowledgment

This research is part of the Bolt and Beautiful project, funded by a subsidy from the Top Sector Energy of the Dutch Ministry of Economic Affairs.

Appendix A. Determination of the axial force and bending moment using strain gauges

Using the coordinate system illustrated in Fig. A1, the normal stress at an arbitrary point i on a circular cross-section under an axial force F_b together with a bending moment M_b acting in the x'-y' plane, may be expressed through superposition of the axial and bending stress components as:

$$\sigma_i = \sigma_{F_b,i} + \sigma_{M_{x'},i} + \sigma_{M_{y'},i} = \frac{F_b}{A_{ut}} + \frac{M_{x'} y'_i}{I} + \frac{M_{y'} x'_i}{I} \tag{A.1}$$

where $A_{ut} = \pi R_b^2$ denotes the cross-sectional area and $I = \pi R_b^4/4$ represents the second moment of area. The components of bending moment about the x' and y' axes are defined as:

$$M_{x'} = M\cos(\theta) \tag{A.2}$$

$$M_{y'} = M\sin(\theta) \tag{A.3}$$

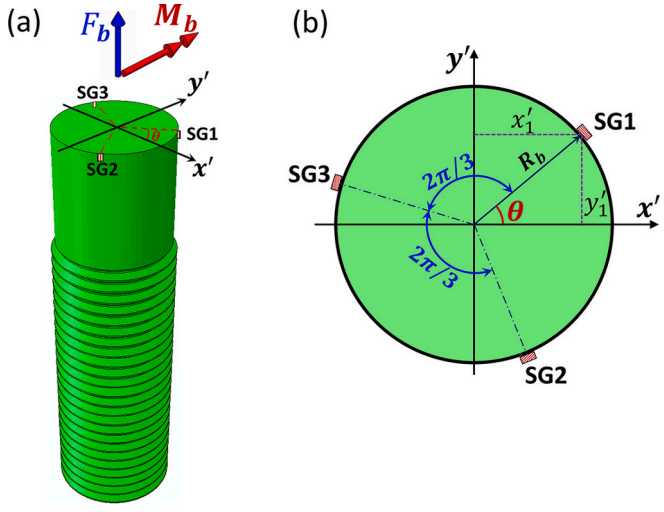

Fig. A.1. (a) Circumferential arrangement of SGs at 120° intervals in the local coordinate system. (b) Cross-sectional view.

The coordinates of the three strain-gauge locations in the local x'-y' system are given by:

$$x'_1 = R_b\cos(\theta), \quad y'_1 = R_b\sin(\theta) \tag{A.4}$$

$$x'_2 = R_b\cos\left(\theta - \frac{2\pi}{3}\right), \quad y'_2 = R_b\sin\left(\theta - \frac{2\pi}{3}\right) \tag{A.5}$$

$$x'_3 = R_b\cos\left(\theta - \frac{4\pi}{3}\right), \quad y'_3 = R_b\sin\left(\theta - \frac{4\pi}{3}\right) \tag{A.6}$$

Introducing the strain relation $\varepsilon_i = \sigma_i/E$ together with the coordinate expressions from equations (A.4)-(A.6) into Eq. (A.1), the measured strains from the three strain gauges can be related to the axial force and bending moment components as follows:

$$\begin{bmatrix}\varepsilon_1\\ \varepsilon_2\\ \varepsilon_3\end{bmatrix} = \begin{bmatrix} \frac{1}{EA_{ut}} & \frac{R_b\sin(\theta)}{EI} & \frac{R_b\cos(\theta)}{EI} \\ \frac{1}{EA_{ut}} & \frac{R_b\sin\left(\theta-\frac{2\pi}{3}\right)}{EI} & \frac{R_b\cos\left(\theta-\frac{2\pi}{3}\right)}{EI} \\ \frac{1}{EA_{ut}} & \frac{R_b\sin\left(\theta-\frac{4\pi}{3}\right)}{EI} & \frac{R_b\cos\left(\theta-\frac{4\pi}{3}\right)}{EI} \end{bmatrix} \cdot \begin{bmatrix} F_b \\ M_{x'} \\ M_{y'} \end{bmatrix} \tag{A.7}$$

Substituting $I = A_{ut}R_b^2/4$ and $R_b = D_{ut}/2$ into Eq. (A.7) yields:

$$\begin{bmatrix}\varepsilon_1\\ \varepsilon_2\\ \varepsilon_3\end{bmatrix} = \frac{1}{EA_{ut}} \begin{bmatrix} 1 & \frac{8\sin(\theta)}{D_{ut}} & \frac{8\cos(\theta)}{D_{ut}} \\ 1 & \frac{8\sin\left(\theta-\frac{\pi}{3}\right)}{D_{ut}} & -\frac{8\cos\left(\theta-\frac{\pi}{3}\right)}{D_{ut}} \\ 1 & \frac{8\cos\left(\theta+\frac{\pi}{6}\right)}{D_{ut}} & -\frac{8\sin\left(\theta+\frac{\pi}{6}\right)}{D_{ut}} \end{bmatrix} \cdot \begin{bmatrix} F_b \\ M_{x'} \\ M_{y'} \end{bmatrix} \tag{A.8}$$

Finally, by inverting the coefficient matrix, the axial force and bending moment components can be determined directly from the measured strains:

$$\begin{bmatrix} F_b \\ M_{x'} \\ M_{y'} \end{bmatrix} = EA_{ut} \begin{bmatrix} \frac{1}{3} & \frac{1}{3} & \frac{1}{3} \\ \frac{D_{ut}\sqrt{3}}{36}\left(-\cos\left(\theta+\frac{\pi}{3}\right)+\sin\left(\theta+\frac{\pi}{6}\right)\right) & \frac{D_{ut}\sqrt{3}}{36}\left(-\cos(\theta)-\sin\left(\theta+\frac{\pi}{6}\right)\right) & \frac{D_{ut}\sqrt{3}}{36}\left(\cos\left(\theta+\frac{\pi}{3}\right)+\cos(\theta)\right) \\ \frac{D_{ut}\sqrt{3}}{36}\left(\sin\left(\theta+\frac{\pi}{3}\right)+\cos\left(\theta+\frac{\pi}{6}\right)\right) & \frac{D_{ut}\sqrt{3}}{36}\left(\sin(\theta)-\cos\left(\theta+\frac{\pi}{6}\right)\right) & \frac{D_{ut}\sqrt{3}}{36}\left(-\sin(\theta)-\sin\left(\theta+\frac{\pi}{3}\right)\right) \end{bmatrix} \cdot \begin{bmatrix}\varepsilon_1\\ \varepsilon_2\\ \varepsilon_3\end{bmatrix} \tag{A.9}$$

Appendix B. Determination of the elastic resilience of the stud and clamped parts

The elastic resilience of the stud (δ_s) and the clamped parts (δ_p) were determined according to the procedures described in VDI 2230 Part 1 [64].

The total stud resilience was calculated as the sum of the elastic deformations of the unthreaded portion, threaded portion and nut engagement regions:

$$\delta_s = \delta_{ut} + \delta_{th} + 2(\delta_G + \delta_M) \tag{B.1}$$

where

$$\delta_{ut} = \frac{l_{ut}}{E_s A_{ut}} \tag{B.2}$$

$$\delta_{th} = \frac{l_{th}}{E_s A_{min}} \tag{B.3}$$

$$\delta_G = \frac{0.5D_{nom}}{E_s A_{min}} \tag{B.4}$$

$$\delta_M = \frac{0.4D_{nom}}{E_s A_{nom}} \tag{B.5}$$

In the above equations, l_{ut}=112 mm and l_{th}=88 mm denote the lengths of the unthreaded and threaded portions within the clamping length, respectively; A_{ut} is the cross-sectional area of the unthreaded section; A_{min} is the cross-sectional area corresponding to the thread minor diameter D_{min}=41.9 mm; and D_{nom}=48 mm is the nominal stud diameter and E_s=210 GPa is the Young's modulus of stud.

Substituting the above values into Eqs. (B.1)-(B.5) yields

$$\delta_s = 9.06 \times 10^{-7}\,\mathrm{mm/N} \tag{B.6}$$

The resilience of the clamped parts was calculated using the deformation-cone method described in VDI 2230 Part 1. The total clamping length was l_K=200 mm. The bolt-hole diameter was d_h=52 mm and the effective bearing diameter under the nut was d_W=92 mm (Fig. B1). The available contact area between the flange segments was approximately 215 × 135 mm. An equivalent available outer diameter of the deformation body was therefore estimated as

$$D_A = \frac{215+135}{2} = 175\,\mathrm{mm} \tag{B.7}$$

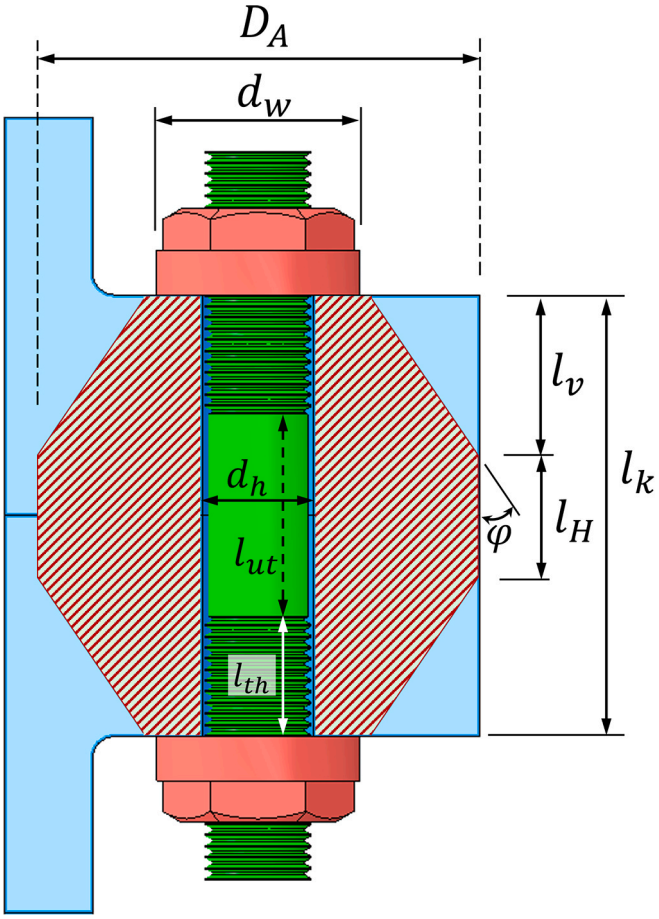

Fig. B.1. Geometrical parameters of the deformation cone and sleeve for a through-bolted joint.

The dimensionless geometric parameters are

$$\beta_L = \frac{l_K}{d_W} = \frac{200}{92} = 2.174 \tag{B.8}$$

and

$$y = \frac{D_A}{d_W} = \frac{175}{92} = 1.902 \tag{B.9}$$

The deformation-cone angle was calculated from

$$\tan\varphi_D = 0.362 + 0.032\ln\left(\frac{\beta_L}{2}\right) + 0.153\ln(y) = 0.463 \tag{B.10}$$

The limiting diameter of the deformation cone is

$$D_{A,Gr} = d_W + l_K\tan\varphi_D = 92 + 200(0.463) = 184.6\,\text{mm} \tag{B.11}$$

Since $D_A < D_{A,Gr}$ the deformation body consists of two deformation cones connected by an intermediate cylindrical sleeve. The cone length is

$$l_V = \frac{D_A - d_W}{2\tan\varphi_D}\,\frac{175 - 92}{2(0.463)} = 89.6\,\text{mm} \tag{B.12}$$

and the corresponding sleeve length becomes (B.13)

$$l_H = l_K - 2l_V = 200 - 2(89.6) = 20.8\,\text{mm}$$

The resilience of the clamped parts is then obtained from

$$\delta_p = \frac{1}{E_p\pi}\left[\frac{2}{d_h\tan\varphi_D}\ln\left(\frac{(d_W + d_h)(D_A - d_h)}{(d_W - d_h)(D_A + d_h)}\right) + \frac{4l_H}{D_A^2 - d_h^2}\right] \tag{B.14}$$

where E_p=210 GPa is the Young's modulus of the clamped parts. Substituting the dimensions of the present connection yields

$$\delta_p = 8.86 \times 10^{-8}\,\mathrm{mm/N} \tag{B.15}$$

The ratio between the stud and clamped-part resiliences is

$$\frac{\delta_s}{\delta_p} = \frac{9.06 \times 10^{-7}}{8.86 \times 10^{-8}} = 10.2 \tag{B.16}$$

indicating that the stud is approximately ten times more compliant than the clamped parts. Consequently, most of the deformation associated with external loading is accommodated through elastic elongation of the stud, while only a relatively small portion is absorbed by deformation of the flange segments.

Data availability

Data will be made available on request.

References

[1] Mehmanparast A, Lotsberg I. Advances in fatigue design of circumferential welds in offshore wind turbine monopile support structures. Eng Struct 2025;337:120445. https://doi.org/10.1016/j.engstruct.2025.120445.

[2] Seidel M, Schaumann P. Calculation of fatigue loads for bolts in eccentrically loaded flanges. Stahlbau 70 (7) (2001) 474-486. (In German) Doi: 10.1002/stab.200101660.

[3] Seidel M, Stang A, Wegener F, Schier C, Schaumann P. Full-scale validation of FE models for geometrically imperfect flange connections. J Constr Steel Res 2021;187:106955. https://doi.org/10.1016/j.jcsr.2021.106955.

[4] Pavlović M, Marković a Z, Veljković b M, Buđevac D. Bolted shear connectors vs. headed studs behaviour in push-out tests. J Constr Steel Res 2013;88:134–49. https://doi.org/10.1016/j.jcsr.2013.05.003.

[5] Seidel M. On design of bolted ring-flange connections of wind turbines, PhD thesis, Universität Hannover, 2001. (In German) Doi: 10.13140/RG.2.2.14685.36328.

[6] Pavlović M, Heistermann C, Veljković M, Pak D, Feldmann M, Rebelo C, et al. Friction connection vs. ring flange connection in steel towers for wind converters. Eng Struct 2015;98:151–62. https://doi.org/10.1016/j.engstruct.2015.04.026.

[7] Schaumann P, Seidel M. Fatigue loads of bolted ring flange connections in wind energy converters. Stahlbau 71 (3) (2002) 204-211. (In German) Doi: 10.1002/stab.200200570.

[8] Mehmanparast A, Lotfian S, Vipin SP. A review of challenges and opportunities associated with bolted flange connections in the offshore wind industry. Metals 2020;10(6):732. https://doi.org/10.3390/met10060732.

[9] Wang S, Su Q, Jiang X, Ghafoori E. Stability of steel columns with bolted strengthening under preload: an analytical model. J Constr Steel Res 2023;201:107699. https://doi.org/10.1016/j.jcsr.2022.107699.

[10] Wang S, Su Q, Jiang X, Ghafoori E. Stability of steel columns with bolted strengthening under preload: experimental study. J Constr Steel Res 2022;190:107119. https://doi.org/10.1016/j.jcsr.2021.107119.

[11] Jian X, Zhou J, Xiang Y, Zhou X, Sun Y, Xu F. High-cycle fatigue performance and life prediction of high-strength lockbolts with pre-tension. J Constr Steel Res 2026;236:109978. https://doi.org/10.1016/j.jcsr.2025.109978.

[12] Shahani AR, Shakeri I. Experimental evaluation of the effect of preload on the fatigue life of bolts. Int J Steel Struct 2015;15(3):693–701. https://doi.org/10.1007/s13296-015-9015-5.

[13] Glienke R, Schwarz M, Hagemann M, Seidel M, Dörre M. Further development of detail categories for bolt-assemblies subjected to normal stress in steel constructions. Ce/Papers 2023;6:1256–62. https://doi.org/10.1002/cepa.2596.

[14] Maljaars J, Euler M. Fatigue S-N curves of bolts and bolted connections for application in civil engineering structures. Int J Fatigue 2021;151:106355. https://doi.org/10.1016/j.ijfatigue.2021.106355.

[15] Glienke R, Hagemann M, Hanebeck R, Schwerdt D, Denkert C, Wegener F, Dörre M. Experimental investigations of the mechanical-technological properties and fatigue strength of stainless steel bolting assemblies. In: Proc. 34th Int. Ocean Polar Eng. Conf., Rhodes, Greece, June 2024, pp. 3124-3132. https://onepetro.org/ISOPEIOPEC/proceedings/ISOPE24/All-ISOPE24/ISOPE-I-24-443/546830.

[16] Seidel M. Flange connections for wind turbine towers in IEC 61400-6 AMD1,. Stahlbau 2025;94(8):486–93. https://doi.org/10.1002/stab.202500024.

[17] Zou T, Niu X, Ji X, Li M, Tao L. The impact of initial imperfections on the fatigue assessment of tower flange connections in floating wind turbines: a review. Front Mar Sci 2022;9:1063120. https://doi.org/10.3389/fmars.2022.1063120.

[18] Seidel M. IEC 61400-6 AMD1 background document: fatigue design for ring flange connections in wind turbine support structures, 2024. Doi: 10.13140/RG.2.2.34114.08645.

[19] Braithwaite J, Goenaga IG, Tafazzolimoghaddam B, Mehmanparast A. Sensitivity analysis of friction and creep deformation effects on preload relaxation in offshore wind turbine bolted connections. Appl Ocean Res 2020;101:102225. https://doi.org/10.1016/j.apor.2020.102225.

[20] Shakeri I, El Bamby H, Tankova T, Veljkovic M. Fatigue life prediction methodology for L-flange connection under different preload levels based on crack growth analysis. Thin-Walled Struct 2025;217:113893. https://doi.org/10.1016/j.tws.2025.113893.

[21] DNV-RP-C203, Fatigue design of offshore steel structures, Det Norske Veritas, Høvik, Norway; 2023.

[22] EN 1993-1-9, Eurocode 3: design of steel structures - Part 1-9: Fatigue, European Committee for Standardization (CEN); 2025.

[23] Schaumann P, Eichstädt R, Stang A. Advanced performance assessment methods for high-strength bolts in ring-flange connections. Stahlbau 2018;87:446–55. https://doi.org/10.1002/stab.201810601.

[24] Lochan S, Mehmanparast A, Wintle J. A review of fatigue performance of bolted connections in offshore wind turbines. Procedia Struct Integr 2019;17:276–83. https://doi.org/10.1016/j.prostr.2019.08.037.

[25] Schwarz M, Glienke R, Wegener F, Seidel M. Fatigue assessment of eccentrically loaded flange connections in wind energy turbines. In: Proc. 33rd Int. Ocean Polar Eng. Conf., Ottawa, Canada, June 2023, pp. 807-814. https://onepetro.org/ISOPEIOPEC/proceedings/ISOPE23/All-ISOPE23/ISOPE-I-23-116/524494.

[26] Rincón-Casado A, Juliá-Lerma JM, García-Vallejo D, Domínguez J. Experimental estimation of the residual fatigue life of in-service wind turbine bolts. Eng Fail Anal 2022;141:106658. https://doi.org/10.1016/j.engfailanal.2022.106658.

[27] Kikuchi Y, Ishihara T. Fatigue prediction of wind turbine tower considering the effect of high-tension bolt failure. Eng Fail Anal 2025;174:109494. https://doi.org/10.1016/j.engfailanal.2025.109494.

[28] Sun L, Liu S, Muhammad U, Zhao H. Study on bolt loosening mechanism under transverse load considering slip and adhesion status of contact surfaces. J Constr Steel Res 2025;224:109149. https://doi.org/10.1016/j.jcsr.2024.109149.

[29] Shahani AR, Shakeri I, Kashani HM. Fatigue life estimation of bolts in flanges of a reinforced cylindrical shell. Modares Mech Eng 2015;14(13):201–8. https://mme.modares.ac.ir/article-15-5808-en.html.

[30] Lin L, Zhao S, Zheng T, Lin Y, Chen NZ, Zhang J. Fatigue assessment for tower bolts of floating offshore wind turbine considering preload loss due to ambient temperature creep. Ocean Eng 2024;313:119527. https://doi.org/10.1016/j.oceaneng.2024.119527.

[31] Sun L, Li L, Gao X. Nonlinear finite element analysis of equivalent Iwan model considering threaded connections. Sci Rep 2025;15:4575. https://doi.org/10.1038/s41598-025-89135-5.

[32] Dörre M, Glienke R, Kalkowsky F, Wegener F, Flügge W. Numerical investigations on the influence of the nominal hole clearance on the plate resilience of high strength preloaded bolted joints. Materialwiss Werkstofftech 2024;55(12):1687–706. https://doi.org/10.1002/mawe.202300382.

[33] Yang G, Zhao H, Yang L, Shao W, Xiao S, Zhu T, et al. Bolt loosening evaluation method based on normalized screw root equivalent stress and loosening life curve. Sci Rep 2025;15:20815. https://doi.org/10.1038/s41598-025-02936-6.

[34] Wang T, Liang G, Liu Y. Mechanical performance analysis of bolt connections for wind turbine towers after corrosion. Struct 2025;71:108202. https://doi.org/10.1016/j.istruc.2025.108202.

[35] Chen J, Dai Y, Jia B, Zheng Y, Huang H. Effect of forced assembly gap on the fatigue behavior of aluminium alloy multi-bolted joints under random loading. Int J Fatigue 2026;203:109344. https://doi.org/10.1016/j.ijfatigue.2025.109344.

[36] Wegener F, Seidel M, Glienke R, Marten F, Schwarz M. Numerical simulation of preload losses of bolts in ring flange connections. Stahlbau 89 (12) (2020) 1003-1015. (In German) Doi: 10.1002/stab.202000055.

[37] Wegener F, Schwarz M, Glienke R, Marten F, Seidel M. Numerical modelling of the force-deformation behaviour of preloaded bolts in L-flange joints. Stahlbau 89 (3) (2020) 266-281. (In German) Doi: 10.1002/stab.201900113.

[38] Buchholz A, Seidel M. Gap height prediction for bolted ring flange connections based on measurements. Steel Constr 2023;16(2):114–26. https://doi.org/10.1002/stco.202200019.

[39] Cheng L, Yang F, Seidel M, Veljkovic M. FE-assisted investigation for mechanical behaviour of connections in offshore wind turbine towers. Eng Struct 2023;285:116039. https://doi.org/10.1016/j.engstruct.2023.116039.

[40] Wegener F, Glienke R, Hinrichs J, Schwarz M, Flügge W. Fatigue strength assessment of large bolting assemblies using the notch-strain approach. Procedia Struct Integr 2025;75:363–74. https://doi.org/10.1016/j.prostr.2025.11.037.

[41] Santa FD, Mehmanparast A. Principal component analysis as an exploratory and diagnostic tool to analyze S-N fatigue trends relevant to offshore wind foundation design. Ocean Eng 2026;343:123236. https://doi.org/10.1016/j.oceaneng.2025.123236.

[42] Annoni A, Johnston C, Mehmanparast A. Fatigue life analysis of threaded connections in offshore wind turbines. Appl Ocean Res 2024;153:104287. https://doi.org/10.1016/j.apor.2024.104287.
[43] He W, Cao S, Hu Z, Xie D, Zhang Z, Wang C. Numerical evaluation on fatigue crack growth and life predictions of an FPSO mooring system. Ocean Eng 2022;265:112501. https://doi.org/10.1016/j.oceaneng.2022.112501.
[44] He W, Xie L, Wang S, Wang C, Hu Z, Liu J. Fatigue characterization analysis of a submerged fishing farm platform through spectral-based fracture mechanics. Ocean Eng 2022;264:112351. https://doi.org/10.1016/j.oceaneng.2022.112351.
[45] Jiao J, Du H, Deng J, Chen P, Lu G. Experimental and theoretical investigation of the high-cycle fatigue failure mechanism of M24 high-strength bolts. J Constr Steel Res 2025;230:109560. https://doi.org/10.1016/j.jcsr.2025.109560.
[46] Zhang P, Li J, Zhao Y, Li J. Numerical simulation and experimental verification of fatigue crack propagation in high-strength bolts based on fracture mechanics. Sci Prog 2023;106(4):1–28. https://doi.org/10.1177/00368504231211660.
[47] Zhang P, Li J, Zhao Y, Li J. Crack propagation analysis and fatigue life assessment of high-strength bolts based on fracture mechanics. Sci Rep 2023;13:14567. https://doi.org/10.1038/s41598-023-41804-z.
[48] Farooq Khan MH, Lee D. Influence of bolt strength in L-type flange joints for wind turbine support structures: an experimental investigation. Struct 2026;84:110968. https://doi.org/10.1016/j.istruc.2025.110968.
[49] ISO 6892-1, Metallic materials - Tensile testing - Part 1: Method of test at room temperature, 2019. https://www.iso.org/standard/78322.html.
[50] ISO 898-1, Mechanical properties of fasteners made of carbon steel and alloy steel, Part 1: Bolts, screws and studs with specified property classes - Coarse thread and fine pitch thread, 2013. https://www.iso.org/standard/60610.html.
[51] ASTM E647-15e1. Standard test method for measurement of fatigue crack growth rates. West Conshohocken, PA: ASTM International; 2015.
[52] Dassault Systèmes, ABAQUS product documentation: ABAQUS analysis user's manual, Version 2023, Dassault Systèmes, Providence, RI, 2023.
[53] VDI 2230 Part 2, Systematic calculation of highly stressed bolted joints - Multi bolted joints, Verein Deutscher Ingenieure; 2014.
[54] Shakeri I, Danielsen HK, Tribhou A, Fæster S, Mishin OV, Eder MA. Effect of manufacturing defects on fatigue life of high strength steel bolts for wind turbines. Eng Fail Anal 2022;141:106630. https://doi.org/10.1016/j.engfailanal.2022.106630.
[55] Zentech International Limited, ZENCRACK User Manual, Version 9.5-1, Zentech International Limited, London; 2025.
[56] Zhang W, Su Y, Jiang Y, Hu Z, Bi J, He W. Data-driven fatigue crack propagation and life prediction of tubular T-joint: a fracture mechanics based machine learning surrogate model. Eng Fract Mech 2024;311:110556. https://doi.org/10.1016/j.engfracmech.2024.110556.
[57] Shakeri I, Farahani EB, Sobhaniaragh B, Eder MA, Kamachali RD, Sarhadi A. Effect of repair welding-induced residual stresses on fatigue crack growth and life of ductile cast iron: application to a full-scale wind turbine hub. Eng Fail Anal 2026;193:110891. https://doi.org/10.1016/j.engfailanal.2026.110891.
[58] Shahani AR, Shakeri I, Rans CD. Fatigue crack growth of Al 5083-H111 subjected to mixed-mode loading. J Braz Soc Mech Sci Eng 2020;42:442. https://doi.org/10.1007/s40430-020-02527-8.
[59] Forman RG, Shivakumar V. Growth behavior of surface cracks in the circumferential plane of solid and hollow cylinders. Fracture Mechanics: Seventeenth Volume, ASTM STP 1986;905:59–74.
[60] Toribio J, Sanchez-Galvez V, Astiz MA, Campos JM. Stress intensity factor solutions for a cracked bolt under tension, bending, and residual stress loading. Eng Fract Mech 1991;39:359–71. https://doi.org/10.1016/0013-7944(91)90050-B.
[61] Mettu SR, de Koning A, Lof C, Schra L, McMahon J, Forman RG. Stress intensity factor solutions for fasteners in NASGRO 3.0. In: Structural integrity of fasteners: second volume, P. Toor, Ed., ASTM International, West Conshohocken, PA, 2000. Doi: 10.1520/STP13530S.
[62] Xu X, Fu P, Zhao J, Wang X, Gong J, Gao G, et al. An improved cyclic plastic model for carbide-free bainitic steel considering the influence of cyclic softening on ratcheting behavior. Int J Fatigue 2025;201:109192. https://doi.org/10.1016/j.ijfatigue.2025.109192.
[63] IEC 61400-6 AMD1, Amendment 1 - Wind energy generation systems - Part 6: Tower and foundation design requirements, 2025. https://webstore.iec.ch/en/publication/82413.
[64] VDI 2230 Part 1, Systematic calculation of highly stressed bolted joints - Joints with one cylindrical bolt, Verein Deutscher Ingenieure; 2015.
[65] API 579-1/ASME FFS-1, Fitness-For-Service, American Petroleum Institute; 2016.
[66] Stolle C, Marten F. Fatigue resistance of large-size high-strength bolts, AiF-Research report 14728 N, Darmstadt/Hannover, 2008. (In German).
[67] Shakeri I, Wu W, Michel A, Eder MA. A model for modifying the S-N curve considering the effect of boundary conditions on the fatigue crack growth of welded components. Fatigue Fract Eng Mater Struct 2024;47:2010–28. https://doi.org/10.1111/ffe.14270.
[68] EN 1990, Eurocode - Basis of structural design, European Committee for Standardization (CEN); 2002.
[69] Shahani AR, Shakeri I, Rans CD. Two engineering models for predicting the retardation of fatigue crack growth caused by mixed mode overload. Int J Fatigue 2020;132:105378. https://doi.org/10.1016/j.ijfatigue.2019.105378.
[70] Maljaars J, Pijpers R, Slot H. Load sequence effects in fatigue crack growth of thick-walled welded C-Mn steel members. Int J Fatigue 2015;79:10–24. https://doi.org/10.1016/j.ijfatigue.2015.04.021.
[71] Shakeri I, Shahani AR, Rans CD. Fatigue crack growth of butt welded joints subjected to mixed mode loading and overloading. Eng Fract Mech 2021;241:107376. https://doi.org/10.1016/j.engfracmech.2020.107376.
[72] Eder MA, Haselbach PU, Mishin OV. Effects of coatings on the high-cycle fatigue life of threaded steel samples. J Mater Eng Perform 2018;27:3184–98. https://doi.org/10.1007/s11665-018-3399-2.
[73] Eichstädt R. Fatigue assessment of large-size bolting assemblies for wind turbine support structures. PhD thesis, Universität Hannover 2019. https://doi.org/10.15488/5157.
[74] Vormwald M. Prediction of crack initiation life based on cyclic fracture mechanics for short cracks, Ph.D. thesis, Technische Hochschule Darmstadt, 1989. (in German).
[75] Haibach E. Fatigue strength - Procedures and data for calculation of structural components], 3rd ed. VDI-Buch, Springer; 2006. (in German) Doi: 10.1007/3-540-29364-7.
[76] Seifi R, Mohammadi MR. Effects of initial overload on the fatigue crack initiation and growth in notched plates. Theor Appl Fract Mech 2024;131:104433. https://doi.org/10.1016/j.tafmec.2024.104433.
[77] Topper TH, Yu MT. The effect of overloads on threshold and crack closure. Int J Fatigue 1985;7(3):159–64. https://doi.org/10.1016/0142-1123(85)90027-1.
[78] Eremin AV, Bogdanov AA, Burkov MV, Panin SV, Sunder R. Effect of periodic overloads on the ΔK threshold estimates in an aluminum alloy. Russ Phys J 2024;67:1992–8. https://doi.org/10.1007/s11182-024-03337-4.